Model space exploration for determining landslide source history from long period seismic data

Pure and Applied Geophysics

Model space exploration for determining landslide source history from long-period seismic data

--Manuscript Draft--

Manuscript Number:	
Full Title:	Model space exploration for determining landslide source history from long-period seismic data
Article Type:	Regular Issue
Keywords:	Landslides; Seismology; Inversion
Corresponding Author:	Laurent Moretti IPGP Paris, FRANCE
Corresponding Author Secondary Information:	
Corresponding Author's Institution:	IPGP
Corresponding Author's Secondary Institution:	
First Author:	Juan Zhao
First Author Secondary Information:	
Order of Authors:	Juan Zhao
	Laurent Moretti
	Anne Mangeney
	Eléonore Stutzmann
	Hiroo Kanamori
	Yann Capdeville
	Eliza Calder
	Clément Hibert
	Patrick Smith
	Paul Cole
	Anne Le Friant
Order of Authors Secondary Information:	
Abstract:	The seismic signals generated by two large volcanic debris avalanches (Montserrat, Lesser Antilles, 1997 and Mount St. Helens, USA, 1980) have been analyzed. Given the times and locations of such landslides, their signals were recorded by only a few seismic stations. Moreover, these signals cover only a very narrow frequency band and include considerable noise. For each event, the source mechanism (i.e. point force) has been determined by waveform inversion using at most two broadband seismic stations. The resulting force is very difficult to interpret in terms of landslide characteristics. A Monte-Carlo inversion was therefore performed by imposing a simple force model associated with the landslide, based on the schematic view of an accelerating/decelerating mass traveling down the slope. The best parameter set of the force model was then found by minimizing misfits and maximizing correlations between data and synthetic signals. This model appears to contain the minimum degree of complexity required to well reproduce the seismic data. The horizontal and vertical components of the resulting force have different source time functions. The best force model compares well with the force obtained by waveform inversion. Finally, this simple force model was interpreted using analytical and empirical relations derived from the sliding block model and granular flow and landslide studies. This made it

	possible to estimate the order of magnitude of the mass, flow duration and direction, initial topography slope, mean velocity and travel distance of the avalanches. For the two avalanches, these calculated characteristics are consistent with field observations.
Suggested Reviewers:	Kate Allstadt allstadt@uw.edu
	Emily Brodsky brodsky@es.ucsc.edu
	Göran Ekström ekstrom@ldeo.columbia.edu
	Robert Sparks steve.sparks@bristol.ac.uk

Model space exploration for determining landslide source history from long-period seismic data

Juan Zhao[1,2], Laurent Moretti[1], Anne Mangeney[1,3], Eléonore Stutzmann[1], Hiroo Kanamori[4], Yann Capdeville[5], Eliza S. Calder[6], Clément Hibert[1,7], Patrick J. Smith[8,9], Paul Cole[8,9], Anne LeFriant[1]

[1]Institut de Physique du Globe de Paris, Sorbonne Paris Cité, Univ. Paris Diderot, UMR 7154 CNRS, Paris, France.

[2]Three Gorges Research Center for Geo-hazard, China University of Geosciences, Wuhan, China.

[3]ANGE team, INRIA, CETMEF, J.-Louis Lions, Paris, France.

[4]Seismological Laboratory, California Institute of Technology, Pasadena, CA, USA.

[5]Laboratoire de Planétologie et Géodynamique de Nantes, Nantes, France.

[6]School of Geosciences, University of Edinburgh, U.K.

[7]Bureau des Recherches Géologiques et Minières, RNSC/RMT, Orléans, France.

[8]Montserrat Volcano Observatory, Flemmings, Montserrat, West Indies, British Overseas Territory.

[9]Seismic Research Centre, University of the West Indies, St Augustine, Trinidad and Tobago.

Abstract The seismic signals generated by two large volcanic debris avalanches (Montserrat, Lesser Antilles, 1997 and Mount St. Helens, USA, 1980) have been analyzed. Given the times and locations of such landslides, their signals were recorded by only a few seismic stations. Moreover, these signals cover only a very narrow frequency band and include considerable noise. For each event, the source mechanism (i.e. point force) has been determined by waveform inversion using at most two broadband

seismic stations. The resulting force is very difficult to interpret in terms of landslide characteristics. A Monte-Carlo inversion was therefore performed by imposing a simple force model associated with the landslide, based on the schematic view of an accelerating/decelerating mass traveling down the slope. The best parameter set of the force model was then found by minimizing misfits and maximizing correlations between data and synthetic signals. This model appears to contain the minimum degree of complexity required to well reproduce the seismic data. The horizontal and vertical components of the resulting force have different source time functions. The best force model compares well with the force obtained by waveform inversion. Finally, this simple force model was interpreted using analytical and empirical relations derived from the sliding block model and granular flow and landslide studies. This made it possible to estimate the order of magnitude of the mass, flow duration and direction, initial topography slope, mean velocity and travel distance of the avalanches. For the two avalanches, these calculated characteristics are consistent with field observations.

1. Introduction

Long-period seismic signals generated by landslides provide unique data to detect gravitational instabilities and to constrain their dynamics [Kanamori and Given, 1982; Kanamori et al., 1984; Kawakatsu, 1989; Brodsky et al., 2003; La Rocca et al., 2004; Favreau et al., 2010; Lin et al., 2010; Moretti et al., 2012; Yamada et al., 2012; Yamada et al., 2013; Allstadt, 2013; Ekström and Stark, 2013]. When flowing over topography, landslides apply forces to the ground surface, generating seismic waves over a wide frequency band. These waves can be recorded far from the source. While seismic energy radiated at short periods is expected to be related to grain impacts and complex momentum exchanges within the mass and with the bedrock, radiation of long-period energy appears to

result from the dynamics of the bulk landslide mass [e.g. La Rocca et al., 2004; Favreau et al., 2010; Hibert et al., 2011, Moretti et al., 2012].

Waveform inversion of the long-period seismic waves can reveal the dynamic history of a landslide [Moretti et al., 2012; Allstadt, 2013; Yamada et al., 2013]. However, this method relies on high-quality seismic data (several broadband seismic stations, low noise, etc.), which are not always available. When only one or two stations are used, such waveform inversion, intended to recover a single force, is usually unstable without a priori information. Furthermore, when the signal can only be observed over a narrow frequency band, the force obtained from waveform inversion is difficult to interpret in terms of landslide properties because of its low temporal resolution. Indeed, the times of the acceleration and deceleration stages, the azimuth of the force that leads to the flow direction and the ratio of vertical to horizontal forces that provides an initial measurement of the slope of the underlying topography are hard to identify on the inverted force, intrinsically filtered in such a narrow frequency band.

From the analysis of the surface wave radiation pattern and spectrum excited by the 1980 Mount St. Helens event, Kanamori and Given [1982] showed that a single horizontal force mechanism was better suited to represent the landslide source than any double-couple mechanism. The source time function of the horizontal single force was first approximated by a bell-shaped curve [Kanamori and Given, 1982]. Deconvolution of the observed seismic signal by the impulse response of the Earth over a frequency band from 0.002 to 0.014 Hz (i.e. 7 s-500 s) showed that the landslide flow history could be approximated as a sinusoidal curve [Kanamori et al., 1984]. Kawakatsu [1989] analyzed the differences between an earthquake and a landslide source and schematically illustrated the effective force generated by a landslide as a sine function. He also proposed a centroid single force (CSF) inversion and applied it to the long-period surface waves generated by massive landslide events. The

CSF solution for the Mount St. Helens landquake (i.e. seismic waves generated by a landslide) was consistent with the geological observations and with the inversion performed by Kanamori and Given [1982]. Going further in the description of the landslide physics, Brodsky et al. [2003] used a sliding block model to represent the temporal changes of the force applied by the landslide to the ground during its trajectory down the slope. By neglecting the vertical force in this model, they deduced that the history of the horizontal force on the ground is similar to a sinusoidal function, with positive and negative peaks related to the acceleration and deceleration stages of the block from the initial destabilization on steep slopes to the arrest on gentle slopes. Since then, the sinusoidal shape of the landslide source time function and CSF inversion have been widely used in source mechanism studies of landslides and glacial earthquakes [e.g. Ekström et al., 2003; La Rocca et al., 2004; Tsai et al., 2007; Lin et al., 2010; Chen et al., 2011]. La Rocca et al. [2004] used three different force source-time functions: a sine wave, a sine wave tapered with a Hanning window and a bell-shaped wave. They deduced the duration of the landslide source from the best normalized cross-correlation between synthetic and observed seismograms. While the resulting synthetic horizontal components fit the data well, the vertical components were poorly reproduced.

In all these approaches, the vertical force was either ignored or taken to be similar to the horizontal force. However, some recent papers have shown that the vertical force can be as large as the horizontal force [Favreau et al., 2010; Moretti et al., 2012; Allstadt, 2013; Ekström and Stark, 2013; Yamada et al., 2013]. While Ekström and Stark [2013] found a similar shape of the source time function for both the horizontal and vertical forces related to the Hunza-Attabad landslide, for other landslides Favreau et al. [2010], Moretti et al. [2012] and Allstadt [2013] have shown that the vertical force may exhibit a very different time history than that of the horizontal force. This is essentially related to the complex interplay between gravity, pressure gradients within the deformable mass, friction and inertial forces

during the flow [e.g. see Figures 13 and 16 in Mangeney-Castelnau et al., 2003]. In particular, centrifugal forces due to 3D topography effects or physical processes such as entrainment of material along the slope significantly affect the source time function of both horizontal and vertical forces (i.e. landslide flow history) [Favreau et al., 2010; Moretti et al., 2012; Allstadt, 2013]. As a result, it is very difficult to define a simple generic landslide flow history model. However, such generic models may be very useful (i) to constrain the waveform inversion of landquakes recorded by a limited number of stations where the use of inversion methods is challenging because the problem is poorly constrained or the noise is high and (ii) to provide simple schemes for the force changes deduced from seismic data, which can be related to the main characteristics of the landslides (mass, direction of the flow, slope angle, duration, etc.). Indeed, data on landslide volume, velocity and direction of the flow can be very useful in remote areas or where field studies are difficult. For example, it can be extremely important to know rapidly if a significant landslide is flowing towards a river, possibly leading to a dam that may subsequently collapse and generate a destructive flood downstream [Petley, 2011, Ekström and Stark, 2013]. Furthermore, recovering the characteristics of past landslides for which no field data are available, over the whole period over which seismic data are available, would provide valuable information to study the time changes of worldwide landslide activity and the link with external forcing such as climate, volcanic or seismic activity.

Extending the simple scheme of an accelerating and decelerating mass flowing down a slope [Brodsky et al., 2003], we propose here a simple impulse force model, considering a pair of forces in opposite directions for both the horizontal and vertical components, independently. This model provides more flexibility than the block model, making it possible to easily change the time and amplitude of each impulse. At the same time, the model is simple enough to be interpreted with a basic understanding of frictional mass flows over topography. We apply this model to two large debris

avalanches that occurred during the volcanic eruption of (1) Soufrière Hills Volcano, Montserrat, Lesser Antilles in 1997 and (2) Mount St. Helens volcano, USA in 1980. Different methods to determine the parameters of this impulse force model (e.g. force amplitudes, time intervals between opposite directions forces, azimuth, etc.) are presented. The aim was to reduce as much as possible the computational time of parameter space exploration, i.e. to find a faster but still well constrained method providing the best fit for the data. The most efficient approach uses the properties of the radiation pattern of horizontal and vertical forces and is based on the calculation of maximum correlation and minimum misfit between synthetic seismic signals calculated with the force model and only a few distant long-period seismic observations (one or two seismic stations located several hundred km from the landslide source).

After discussing the force model in Section 2, we detail in Section 3 the application of these methods to the challenging case of the Boxing Day debris avalanche in Montserrat where only two seismic stations were available, one with a poor signal to noise ratio in particular due to the presence of other events. In Section 4, we apply our method to the Mount St. Helens landquake and compare the results to former studies of this event. For both debris avalanches, the best method was able to recover the direction of flow, mass, duration, mean velocity and travel distance of the landslide as well as the mean slope angle of the topography during the initial avalanche motion, in agreement with field observations.

2. Source model with impulse forces

Because here the length of the landslide is small compared to the wavelength of the seismic waves and the distances to the seismic stations, we assume a point source force. Brodsky et al. [2003]

provided the basis for a simple understanding of the force generated by a landslide during its travel along the topography by comparing it to a rigid block sliding along a varying slope. When moving, the block is subjected to two forces acting in the slope-parallel direction: the projection of the gravity force along the slope and the basal friction, assumed to be a Coulomb friction force in the opposite direction to the sliding motion. In the direction perpendicular to the slope, the bed reaction balances the weight of the block (see Figure 1a). As a result, if centrifugal acceleration due to the slope curvature is neglected (e.g. see Section 6.1 of Mangeney-Castelnau et al., 2003), the equations of motion of the block in the reference frame tangent to the topography (X, Z) are:

$$\begin{cases} M\gamma_X(t) = Mg\sin\theta(t) - \mu Mg\cos\theta(t) & (1) \\ M\gamma_Z(t) = 0 & (2) \end{cases}$$

where $\boldsymbol{\gamma}$ is the block acceleration, μ the Coulomb friction coefficient, M the mass of the block, $\mathbf{g}$ acceleration due to gravity and $\theta(t)$ the slope angle of the bedrock under the center of gravity of the block at time t. Note that the vectors are represented here by bold letters. When the gravity force is higher than the friction force (i.e. at the beginning of the sliding on steep slopes), the block accelerates and, when reaching gentler slopes, friction overcomes gravity and the block decelerates until it stops. During the flow, the force applied by the block to the ground is the opposite of the friction force in the slope-parallel direction and is equal to the weight of the block in the slope-perpendicular direction. In the horizontal/vertical reference frame (x,z), the force applied by the block to the ground can be expressed as

$$\begin{cases} F_x^{M\to G}(t) = Mg\cos\theta(t)(\mu\cos\theta(t) - \sin\theta(t)) & (3) \\ F_z^{M\to G}(t) = -Mg\cos\theta(t)(\mu\sin\theta(t) + \cos\theta(t)) & (4) \end{cases}$$

The variation of the force applied by the mass to the ground surface $\Delta\mathbf{F}$ is the difference between the force at the equilibrium state where $\mathbf{F}_e{}^{M\to G} = M\boldsymbol{g}$, and the force during the flowing state (Equations (3)-(4)). In the horizontal/vertical reference frame (x,z), $\Delta\mathbf{F}$ can be expressed as

$$\begin{cases} \Delta F_x(t) = Mg\cos\theta(t)(\mu\cos\theta(t) - \sin\theta(t)) & (5) \\ \Delta F_z(t) = -Mg\sin\theta(t)(\mu\cos\theta(t) - \sin\theta(t)) & (6) \end{cases}$$

The ratio between the vertical and horizontal force variation, respectively Equations (5) and (6), is:

$$\frac{\Delta F_z}{\Delta F_x}(t) = -\tan\theta(t) \qquad (7)$$

For example, the force corresponding to Equations (5) and (6) is shown in Figure 1b for a block sliding over a topography profile extracted from the White River Valley Digital Elevation Model in Montserrat where the Boxing Day avalanche occurred. As can be observed in this figure, during the acceleration stage, the landslide motion results in a slope parallel force applied to the ground that is in the opposite direction of the flow. On the other hand, during the deceleration stage, the force is in the sliding direction. Note that the force is always tangent to the topography (see Equations (1)–(2)) and that this simple block model predicts a change of the sign of the horizontal and vertical forces at the same time. Taking into account the centrifugal force would change this scheme but would significantly

complicate the model by introducing the block velocity and the curvature radius of the topography [e.g. see equations (61) and (62) in Mangeney-Castelnau et al. 2003].

In Figure 1c, we show the force calculated using a simulation of a mass spreading on the same topography profile as in Figure 1b. The simulation was performed using the SHALTOP model that describes thin granular flows over complex topography taking into account in particular centrifugal forces, pressure gradients and a Coulomb friction law [Bouchut et al., 2003; Mangeney et al., 2007; Moretti et al., 2012]. Figure 1c shows that, in this case, the associated force is qualitatively similar to that obtained using the sliding block model, involving an acceleration and deceleration phase. However, it is no longer tangent to the topography. Using inversion of seismic data and numerical modeling of landslides over complex 3D topography, Favreau et al. [2010] and Moretti et al. [2012] have shown that the landslide force history is more complex (e.g. see Figure 3a-c in Moretti et al., [2012]). This is due to other forces such as pressure gradients related to the deformable mass and the presence of centrifugal forces related to the radius of curvature of the topography [Favreau et al., 2010, Allstadt, 2013] or to physical processes such as the presence of a glacier or the entrainment of slope material during the flow [Moretti et al., 2012].

In order to keep the force model simple while allowing more degrees of freedom than those of the simple block model, we defined a model with both horizontal and vertical components, each made up of two parallel forces in opposite directions, separated by different time intervals (Figure 1d). We decided here to use impulse forces for simplicity although sinusoidal or boxcar curves could also have been used [La Rocca et al., 2004; Tsai et al., 2007] (see Figure 1d). Because of the filtering of the data and of the synthetic signals, we expect to obtain similar force models using any of these source time functions. The force model is reduced to two impulse forces in opposite directions of amplitudes A_{h1} and A_{h2} at times t_1 and t_2, respectively, for the horizontal component, and of amplitudes A_{v1} and A_{v2} at

times t_1 and t_3, respectively, for the vertical component. Note that the first horizontal and vertical pulses are assumed to occur simultaneously (Figure 1d). As a result, the model has 8 unknowns (A_{h1}, A_{h2}, t_1, t_2, A_{v1}, A_{v2}, t_3, ϕ), where ϕ is the azimuth of the horizontal force.

An important issue is to know the minimum complexity that must be taken into account in the force model to be able to reproduce the data. To investigate this, we tried to simplify the above model by testing force models (i) using the same time delay between the two pulses (t_2=t_3) and the same amplitude ratio between the second and first pulse for the horizontal and vertical forces pulses ($A_{h1}/A_{h2}=A_{v1}/A_{v2}$), (ii) imposing only the same time delay between the two pulses of the horizontal and vertical pulses (t_2=t_3). Neither of these models well reproduced the observed seismic signal for the two avalanches studied here (Montserrat, Lesser Antilles and Mount St. Helens, USA).

3. The 1997 Boxing Day debris avalanche, Montserrat

On 26 December 1997, at ~03:00h local time, the southern retaining crater wall of the Soufrière Hills Volcano, Montserrat (16.71°N, 62.18°W) collapsed, undermining a large (~113 Mm^3) actively-growing lava dome [Sparks et al., 2002; Voight et al., 2002]. The collapse formed a debris avalanche that traveled 4.5 km down the White River Valley to within a few hundred meters of the coastline. The debris avalanche was immediately followed by high-energy pyroclastic density currents that resulted from collapse and fragmentation of the lava dome, which subsequently overran the debris avalanche and swept out to sea. The event completely devastated an area of 10 km^2 covering a 70° sector of southern Montserrat (Figure 2a) and even generated a small (1-2 m) tsunami.

There were no direct observations of the event, as it took place at night, but aspects of the deposits combined with the time at which the seismic stations stopped transmitting, provide a number of

constraints on the chronology and dynamics of the events [Sparks et al., 2002; Voight et al., 2002]. The collapse of the retaining crater wall, Galway's Wall, was directed south, principally down the White River Valley, although it overspilled the valley walls at two bends. Superelevation effects indicate that the debris avalanche in the White River channel had a minimum velocity of 35 m/s. The deposit is made up of four main imbricated units, with the lower units made up of material originating deeper in the edifice, closer to the failure plane, and the upper units dominated by unconsolidated talus. The pyroclastic density current was directed to the southwest, along an axis 1.5 km to the north of the White River Valley (i.e. slightly oblique with respect to the debris avalanche direction). It was generated during 12 minutes of intense seismic activity by pulsatory, retrogressive failure of the lava dome and the deposits show widespread evidence of two main depositional units. The debris avalanche deposit was clearly already emplaced when it was overrun by the pyroclastic density current [Sparks et al., 2002]. The volumes of the collapsed material are constrained by estimates of the volumes of the resulting scars as well as independent estimates of the volumes of material emplaced in the downstream drainage system. The volume of the debris avalanche, mostly made up of old material collapsed from the edifice, is estimated at $40\text{-}50\times10^6$ m^3 [Voight et al., 2002], while the volume of the pyroclastic density current that was formed by the resulting collapse of the lava dome was $35\text{-}45\times10^6$ m^3. The estimated total failure volume is given by Sparks et al. [2002] as $80\text{-}90\times10^6$ m^3.

A seismometer array had been installed on Montserrat island. During 1996-1998, a broadband network and a short-period network ran in parallel, consisting of five 3-component broadband seismometers (Guralp CMG-40T) and three vertical-only Integra LA100/F 1 Hz short-period instruments. However, on 26 December 1997, only two seismic stations with short-period instruments (MBLG and MBWH, Figure 2a) were functioning and able to transmit their vertical component seismograms to the observatory.

The long-period seismic signals generated by the avalanche were recorded by only two distant three-component broadband seismometers from the Global Seismographic Network (GSN): SJG located in Puerto Rico and SDV located in Venezuela, 450 km and 1262 km from the avalanche, respectively (Figure 2b).

3.1. Time duration and frequency band chosen for analysis of the long-period surface waves

Sparks et al. [2002] analyzed the local short-period seismogram of the Windy Hill seismic station (MBWH) from 24 to 26 December 1997. They performed Real-time Seismic Amplitude Measurements (RSAM) and fixed the starting time of the collapse event (07:01, UT) at the RSAM spike. They also analyzed the most emergent and pulsating part of the data, which lasts about fifteen minutes (Figure 3). This part of the signal was attributed to the collapse and divided into six main pulses. They attributed the first two main pulses of the seismogram to the debris avalanche event.

From the spectrograms of the signals at both MBLG and MBWH, located 2.5 km and 3.7 km from the dome, respectively, energy gaps that divide the signal into six parts can be observed (Figure 3a-b). The starting times of these intervals are marked T1 to T6 (Figure 3). These times are consistent with the analysis of Sparks et al. [2002]. The first two pulses (between marks T1 and T3) together last about 180 s which is assumed to be the duration of the debris avalanche (Figure 3).

Particle motion calculated from the radial and vertical components at distant stations SJG and SDV shows that most of the signal consists of Rayleigh waves in the radial and vertical direction (Figures 4b,c,d and 4f,g,h) and Love waves in the transverse direction (Figure 4a and 4e). Surface wave travel time is calculated based on the group velocity from the Preliminary Reference Earth Model (PREM

[Dziewonski and Anderson, 1981]): 3.88 km/s for the Rayleigh waves at 50 s, 3.34 km/s for the Rayleigh waves at 20 s, 4.19 km/s for the Love waves at 50 s and 3.43 km/s for the Love waves at 20 s. The arrival times of the first two main pulses and the sixth main pulse are marked in Figure 4. The first two main pulses can be identified in the 3-component seismograms and spectrograms of both SJG and SDV. The sixth main pulse, at the end of this eruptive event, can only be identified at the closest station SJG. Its imprint on the vertical component is much stronger than on the transverse component, which is consistent with the radiation pattern of a single vertical force [Kanamori and Given, 1982]. As discussed by Sparks et al. [2002], this last pulse in the signal is possibly generated by a final explosive phase. Pulses 3 to 5 are not visible at SJG. A field survey suggests that these pulses are related to the pyroclastic density currents that occurred just after the debris avalanche. One possible explanation would be that these currents generated fewer low frequency signals. This is however impossible to check because the local seismometers are only short-period (>1 Hz). As high frequencies are much more attenuated than low frequencies, this could explain why it is difficult to observe them at such large distances.

Ideally, broadband seismograms are necessary for a well constrained waveform inversion [Chen et al., 2011]. Unfortunately, the signal at the SDV station, especially for the transverse component, is too noisy at periods <25 s and >40 s. As a result, we can only deal with signals filtered between 25 s and 40 s, where the waveform is relatively clean at both stations. Because of the poor signal to noise ratio of the horizontal components of SDV, we only use the 3 components of SJG and the vertical component of SDV, filtered with a zero-phase Butterworth filter (acausal).

3.2. Waveform inversion

Using the filtered velocity record, we performed a waveform inversion to find the force applied by the landslide to the ground. The seismograms at a given station are the result of the convolution of the source time function and the Green's functions.

$$S_i(t) = G_{i,j}(t) * F_j(t) \qquad (8)$$

where $S_i(t)$ is the seismic signal, $G_{i,j}(t)$ are the Green's functions, $F_j(t)$ is the three-component source force and i,j=E,N,Z are the 3 directions in space. Based on the one-dimensional PREM model, we used the normal mode summation method [Gilbert and Dziewonski, 1975] to generate Green's functions. Then we performed a Fourier transform on both seismograms and Green's functions, turning the deconvolution problem in the time domain into a problem of solving a linear system of equations in the frequency domain. We then solved the system of equation using the least-squares method. Finally we performed an inverse Fourier transform to get the source time function. The resulting force has mostly north and vertical components (red lines in Figure 5a). It is however difficult to extract the time history of the horizontal and vertical components from the force filtered in this very narrow frequency band. Using only the SJG station or the SJG station and the vertical component of SDV in the inversion process gives very similar results, suggesting that the waveform inversion using only one station may be well constrained (Figure 5a).

3.3. Strategy for parameter space exploration

To determine the main forces that could represent the avalanche dynamics, let us find the system of impulse forces (see section 2) that may explain the observed signal at the two distant stations SJG and

SDV. The method proposed here essentially consists of calculating the synthetic seismograms generated by the horizontal and vertical forces, each composed of two pulses (Figure 1d). This model involves 5 unknown parameters for the horizontal force (t_1, A_{h1}, t_2, A_{h2}, azimuth ϕ) and 3 unknown parameters for the vertical force (A_{v1}, A_{v2}, t_3). For each station, a time shift is also introduced to take into account the Rayleigh wave arrival time delay dt_{SJG} and dt_{SDV}. Indeed, we need to correct the arrival time at each station with respect to the theoretical arrival time calculated from the PREM 1D Earth model because of the different structures crossed by the waves in their path to SJG and SDV. For these stations located 450 km and 1262 km from the source, respectively, we vary the Rayleigh wave arrival time t_{ri} by 20 seconds around t_{pi}, where t_{pi} is the arrival time at station i=SJG, SDV calculated from PREM: $t_{ri} \in [t_{pi}\text{-}10\text{ s}, t_{pi}\text{+}10\text{ s}]$. This introduces two more parameters in the model, now defined by 10 parameters. The range of values investigated for each parameter is given in Table 1.

We test here three different approaches to finding the best parameter set by reducing as much as possible the computational time of the model space exploration. The idea is to find a faster but still well constrained method that provides the best fit for the data. All the approaches are based on the Monte-Carlo sampling method [Sambridge, 2002; Tarantola, 2005] that consists of randomly choosing the 10 parameters of the model. This gives a force model, which we filter in the same frequency band as the data. Then the associated synthetic seismograms are calculated using Normal Mode Summation and compared with real data on the basis of calculating correlation and misfit between synthetic seismograms and data. We define criteria such as maximizing the correlation and minimizing the misfit between synthetic seismograms and data. The models are then sorted from the best to the worst, according to each criterion separately. Finally, the best model is the first that appears in all the vectors of sorted models. The normalized correlation is calculated as

$$C = \frac{\sum_{i=1}^{N}(x_i - \bar{x})\cdot(y_i - \bar{y})}{\sqrt{\sum_{i=1}^{N}(x_i - \bar{x})}\cdot\sqrt{\sum_{i=1}^{N}(y_i - \bar{y})}} \qquad (9)$$

and the misfit as

$$misfit = \sqrt{\frac{1}{N}\sum_{i=1}^{N}(x_i - y_i)^2} \qquad (10)$$

where x and y are the two signals for which the correlation and misfit are calculated, respectively.

In the first approach, the inversion was carried out simply by randomly choosing the 10 parameters using the Monte-Carlo sampling method (10^8 iterations requiring about 4 days on an Intel E6850 3 GHz processor using MATLAB). We choose the following criteria to sort the models: maximum correlation and minimum misfit on the radial, transverse and vertical components at SJG and on the vertical component at SDV, providing 8 different vectors of sorted models. The resulting 10 best models, shown in Table 2, are quite different from one another. There is indeed a large dispersion of the parameter values showing that the solution is poorly constrained (see Figure S1 in the supplementary material). For almost all the parameters, the ten best values are not clustered around one value but rather belong to several groups of parameter values. A more obvious maximum may have been found by increasing the number of iterations. However, to explore at least 10 values for each parameter would require 10^{10} iterations (several months of calculation). To reduce the computation time, we propose a different strategy.

3.3.1. Reduction of the number of parameters using the transverse component

The main idea is to use the radiation pattern properties of waves generated by a force (Figure 6) to separate the inversion into two steps. As a vertical force does not generate Love waves (vertical forces only generates motion in the radial and vertical directions), the transverse component only results from the horizontal force [Kanamori and Given, 1982], which depends on 5 parameters (t_1, t_2-t_1, A_{h2}/A_{h1}, A_{h1}, ϕ). The amplitude A_{h1} and the azimuth of the force ϕ modify only the amplitude of the seismic signal recorded on the transverse component. They do not affect the value of the correlation between data and synthetic signals. The correlation can only change sign if the force acts in the opposite direction (Figure 7c). As a result, only the 3 parameters t_1, t_2-t_1, A_{h2}/A_{h1} of the force model could affect the absolute value of the correlation on the transverse component. We calculated the correlation between the recorded and synthetic transverse component of SJG (SJG-T) by systematically varying these 3 parameters. For this step, we performed 10^6 iterations. The projection of this 3D calculation on the t_1-axis shows that the maximum correlation C=0.946 is obtained for t_1=80 s (Figure 7a). For this value of t_1, Figure 7b shows the point where the maximum correlation is obtained, corresponding to t_2-t_1=69 s and A_{h2}/A_{h1}= -0.7. For these parameter values, half of the azimuth range gives positive correlation values, while the remaining half of the range gives negative values (Figure 7c). This makes it possible to reduce the possible range of azimuths to $\phi \in$ [-69,110]°.

3.3.2. Determination of the remaining parameters

With t_1=80 s, t_2=149 s and A_{h2}/A_{h1}= -0.7 fixed by the above calculation, we performed a second

step to search for the remaining 7 parameters of the model: t_3-t_1, A_{h1}, A_{v1}/A_{v2}, A_{v2}/A_{h1}, dt_{SJG}, dt_{SDV} and the azimuth ϕ. We used two different methods to find these parameters, based on the following criteria:

Method a: Maximum correlation and minimum misfit between synthetic signals and data.

Method b: Maximum correlation and minimum difference of the Rayleigh to Love wave amplitude ratio between synthetic signals and data (ratio between vertical and transverse components). This method makes it possible to reduce the number of parameters to 6. Indeed, the correlation and the amplitude ratio are not sensitive to the absolute amplitude. As a result, we can fix the value of A_{h1} and only calculate A_{h2}/A_{h1}, A_{v1}/A_{v2} and A_{v2}/A_{h1}. The absolute amplitude A_{h1} will be found in the end using the linearity properties of wave equations (see Section 3.3.2.2).

We have investigated these two methods to evaluate how Method b, that decreases the computational time by reducing the number of parameters, compares to Method a, that uses the amplitude of the full waveform but requires about 10 times more computational time for the same parameter space sampling.

3.3.2.1 Method a: Using correlation and misfit as inversion constraints

In Method a, the criteria are maximum correlation and minimum misfit between data and synthetic signals. For this step, we performed 10^7 iterations. The 10 best models are given in Table 3 (the corresponding misfits and correlations are given in the supplementary material, see Table S1). Figure 8 shows that the parameters are quite well constrained with an overall small dispersion of the parameter values for the 10 best models, except for the two parameters A_{v2}/A_{h1} and A_{v1}/A_{v2}. The values obtained for the best model are t_3-t_1=41 s, A_{h1}=1.68×10^{10} N, A_{v1}/A_{v2}=-0.60, A_{v2}/A_{h1}=0.71, dt_{SJG}=-3 s, dt_{SDV}=5 s and the azimuth ϕ=19.74°. The mean values and standard deviations of the parameters corresponding

to the 10 best models are given in Table 3.

3.3.2.2 Method b: Using correlation and amplitude ratio as inversion constraints

In Method b, we only need to retrieve 6 parameters (t_3-t_1, A_{v1}/A_{v2}, A_{v2}/A_{h1}, dt_{SJG}, dt_{SDV} and ϕ). The constraints here are the maximum correlation and the minimum difference of the Rayleigh to Love wave maximum amplitude ratio between data and synthetic waveforms. Here, to obtain the same sampling of the model space as in Method a, we performed 10^6 iterations. Once the inversion was done, the absolute amplitude of the force (A_{h1}) still had to be determined. To do that, we simply generated source time functions according to the force model with the six inverted parameters, with the amplitude fixed to $A_{h1}=1\times10^{10}$ N, and calculated the associated synthetic waveforms. Comparison between synthetic waveforms and observations shows that the amplitude of the observed seismograms is about 1.53 times the synthetic seismograms amplitude on average. Because this is a linear elastic problem, this implies that $A_{h1}=1.53\times10^{10}$ N. The amplitudes A_{h2}, A_{v1} and A_{v2} can then be directly deduced from this value. This method gives less accurate results than Method a, with overall lower correlation values and higher misfits. Furthermore, there is a large dispersion of the parameter values for the 10 best models. We tried to increase the number of iterations to 10^7, i.e. the same number of iterations as in Method a. This provides a finer sampling of the parameter space than in Method a. In that case, we obtained results very close to those of Method a. Only the poorly constrained parameters A_{v2}/A_{h1} and A_{v1}/A_{v2} are really different. The 10 best models are given in Table 4 (the corresponding misfits and correlations are given in the supplementary material, see Table S2). The values obtained for the best model are t_3-t_1=40 s, $A_{h1}=1.8\times10^{10}$ N, A_{v1}/A_{v2}=-0.3, A_{v2}/A_{h1}=1.07, dt_{SJG}=-3 s, dt_{SDV}=4 s and the azimuth ϕ=11°.

3.3.3 Final model

We obtained very consistent results with Methods a and b when 10^7 iterations were performed, much better than those obtained by simply varying the 10 parameters involved (see beginning of section 3.3). Method a gave slightly better results (Table 5) but our results suggest that Method b can be used when the full waveform is noisy if the maximum amplitudes are still clearly defined. The stability of the results, whatever the method, possibly supports the use of a simple three-component-two-pulse force model for the inversion of the landslide source. Finally, for the 1997 Boxing Day debris avalanche event, the impulse force model obtained by the slightly more accurate Method a (Figure 9a) is composed of:

1 - A horizontal force: $A_{h1}=1.68\times10^{10}$ N at $t_1=80$ s and $A_{h2}=-1.18\times10^{10}$ N at $t_2=149$ s, with azimuth $\phi=19.7°$

2 - A vertical force: $A_{v1}=0.72\times10^{10}$ N at $t_1=80$ s and $A_{v2}= -1.19\times10^{10}$ N at $t_3=121$ s.

The 3-component landslide flow history obtained with this model, filtered between 25-40s, compares well with the force calculated using waveform inversion of the observed data, as shown in Figure 9b. It is interesting that such good agreement is obtained between these different methods, especially with the waveform inversion obtained using only one station. This may suggest that waveform inversion to recover a single force is actually well constrained, even with only one seismic station. The filtered force is then used to generate synthetic waveforms that well reproduce the recorded waveforms at both stations (Figure 10). The synthetic seismic signals generated by the 10 best models are shown in the supplementary material (Figure S2).

Our method is based on the determination of 3 parameters using the transverse component of the seismic signal. These parameters are held constant to determine the remaining parameters. We performed some stability tests by repeating the second step of the inversion while letting these 3 parameters slightly vary around their best values: t_1=80±5 s, t_2-t_1=69±5 s and A_{h2}/A_{h1}=-0.7±0.1. For each parameter, we give the mean value and the standard deviation corresponding to the 10 best models obtained: t_1=79.6 s ± 0.7 s, t_2-t_1=68.8 s ± 1.2 s, t_3-t_1=39.1 s ± 1.7 s, A_{h2}/A_{h1}=-0.73 ± 0.07, A_{v1}/A_{v2}=-0.95 ±0.22, A_{v2}/A_{h1}=0.58 ± 0.18, ϕ=18.8° ± 5.62° and A_{h1}=1.63×10^{10} N± 0.28×10^{10} N. As can be seen, the inversion is well constrained for most of the parameters.

3.3.4 From the force to landslide characteristics

Note that the azimuth of the horizontal force (19.7°) is very close to the global orientation of the White River Valley and opposite to the avalanche flow direction (approximately 201°=21°+180°) (Figure 2a) as predicted by the block model. Using Equation (7) leads to a slope angle θ=arctan(A_{v1}/A_{h1})=23°, which could give an estimate of the initial slope. In fact, the maximum slope over which the debris avalanche flowed was 30° and the mean slope at the beginning of the valley was 20° (values extracted from the Digital Elevation Model). Equation (5), similar to Equation (1) in La Rocca et al. [2004] (deduced from Brodsky et al. [2003]), suggests that the mass of the debris avalanche could be calculated from the amplitude of the horizontal force

$$M = \left| \frac{F_h}{g(\mu \cos\theta - \sin\theta)\cos\theta} \right| = \alpha \cdot F_h \qquad (11)$$

Here F_h=A_{h1}=1.68×10^{10} N, and we can approximate the slope angle at θ=23°, as deduced from Equation (7). Simulation of landslides of this size requires values of the friction coefficient typically of the order of μ=tan(δ)=tan(15°)=0.27 [e.g. see Pirulli and Mangeney, 2008; Lucas et al., 2013]. Using these values in Equation (11) gives

$$M = 0.77F_h \qquad (12)$$

By varying the parameters (θ or δ) by 10%, Equation (11) gives a proportionality coefficient included in the range $\alpha \in [0.53\ 1.47]$. This empirical coefficient is a little higher but consistent with the empirical fit found by Ekström and Stark [2013] for a compilation of large landslides (M=0.54 F_h). With these coefficients, the calculated mass would be 0.89×10^{10} kg<M<2.47×10^{10} kg. The volume involved in the Boxing Day debris avalanche has been estimated from field studies to be V=40-50 Mm^3. With a density ρ=1980 kg/m^3 [Voight et al, 2002], this gives a mass of M=7.9×10^{10}-9.9×10^{10} kg. As a result, the mass deduced with Equation (12) is at least 3 times smaller than the expected mass, but it provides an order of magnitude estimate of the real mass. Using the empirical relation from Ekström and Stark [2013] would lead to an even smaller mass. Figure 2 of Ekström and Stark [2013] suggests an uncertainty in the mass determination from the maximum force value of about 50% (i.e. 5×10^9 kg) for landslides of about M≈1×10^{10} kg. Our result suggests a much larger uncertainty which could be due to the strong impact of topography and physical processes such as erosion/deposition on the generated seismic signal [Favreau et al., 2010; Moretti et al., 2012]. Another possibility would be that the debris avalanche was made of several events of smaller volumes or at least a highly unsteady event. However, this would probably generate a more complex seismic waveform.

The approximate duration of the force (about 100-200 s) is about the same as that expected for the Boxing Day debris avalanche [Sparks et al., 2002]. The duration of the landslide appears to roughly correspond to twice the time interval between the two horizontal impulse forces (see Figure 1d). This time interval is 69 s so that the landslide duration would be about 140 s (Figure 9a).

Laboratory experiments on granular flows and simulations of real landslides suggest that the order of magnitude of the mean velocity of the granular mass is

$$U = \sqrt{g h_0 \cos\theta} \qquad (13)$$

[Roche et al., 2008, Farin et al., 2013, Lucas et al., 2013], where h_0 is the initial thickness of the released mass. Empirical laws relating h_0 to the landslide volume for very well constrained data [Lucas et al., 2013], show that

$$h_0 \approx 0.45 \times V^{0.32} \qquad (14)$$

As a result, the mean velocity is in the range 23 m/s<U<28 m/s. From landslide data from Legros [2002], Lucas et al. [2013] proposed an empirical relation between the runout distance R and the volume V:

$$R = 6 \times V^{0.37} \qquad (15)$$

With the volume deduced from seismic data, we find a runout distance of 1.7 km<R<2.5 km. On the other hand, with the velocities calculated above and the estimated time of the landslide, we can roughly

calculate the distance L traveled by the center of mass using the simple formula $L = U \times t$. This gives 3.24 km<L<3.89 km. Field observations suggest U≈35 m/s and a runout distance (maximum distance traveled by the mass) R≈4.5 km. Note that field observation generally provides the runout distance and not the center of mass travel distance. As a result the calculated values of travel distances and velocity are slightly lower than observations, but again provide an order of magnitude of the real values.

4. The 1980 Mount St. Helens eruption

On 18 May 1980, at 15:32 (UT), the failure of the north flank of the Mount St. Helens volcano (46.21°N, 122.19°W) caused a catastrophic eruption. A massive debris avalanche with a volume of about 2.8×10^9 m^3 was generated. Its scar went down nearly to the base of the volcanic cone on the north side and it moved down the lower gradients of the volcano's outer flank [Christiansen et al., 1981]. Part of the avalanche was blocked by a ridge 8 km to the north, but the bulk of the avalanche turned westward down the valley of the North Fork Toutle River (Figure 11a). As for the Montserrat eruption, the Mount Saint Helens debris avalanche was followed by a pyroclastic flow with a volume of about 0.25 km^3 that covered the debris avalanche deposits with a thickness of about 40 m (Figure 11a). The long-period seismic waves generated by the debris avalanche were recorded at many stations. Kanamori et al. [1984] inverted these data to find the force representing the avalanche. Seismograms at stations ANMO (1820 km away) and GRFO (8470 km away) have clean waveforms in the period 100-250 s and could be used to perform the Monte-Carlo inversion on the Mount Saint Helens debris avalanche (Figure 11b). Note that, contrary to Montserrat, we can use the transverse components of the two stations.

We applied the method described previously for the Montserrat debris avalanche (see section 3.3.1

and 3.3.2). In the first step, the transverse component of each station was used separately. The values of t_2 and A_{h2}/A_{h1} are similar for the two stations while the values of t_1 identified are 65 s for ANMO and 23 s for GRFO. The difference in the determination of t_1 could be due to the Love wave arrival time difference between the real value and the one calculated from PREM. Because station ANMO is closer to the source (1820 km away), we assume that, for ANMO, there is no difference between the real Love wave arrival time and the calculated time from PREM. For GRFO, the arrival time difference is 65 s-23 s=42 s. We then performed the inversion on the remaining parameters. We obtained a Rayleigh wave arrival time difference of -27 s for GRFO (no difference for ANMO). These time shifts correspond to a maximum wave velocity difference, with respect to the PREM model, of 2.2%. The best model is found, as for the Montserrat debris avalanche, using Method a (Table 6). The resulting force model is made up of a horizontal force (A_{h1}=4.01×10^{12} N at t_1=65 s and A_{h2}= -4.01×10^{12} N at t_2=155 s, with azimuth ϕ=186°) and a vertical force (A_{v1}=0.62×10^{12} N at t_1=65 s and A_{v2}=-1.16×10^{12} N at t_3=93 s). The dispersion of the parameters for the 10 best models is quite small as shown in Figure 12. The final single force model for the Mount St. Helens debris avalanche is shown in Figure 13a. The three components of the landslide flow history (i.e. source time function), filtered between 100-250 s, compare well with the force calculated using waveform inversion (Figure 13b). The force model is then used to generate synthetic waveforms that also well reproduce the recorded waveforms (Figure 14).

The azimuth of the horizontal force (186°=6°+180°) is very close to the global orientation of the first part of the valley where the debris avalanche flowed and is opposite to the flow direction (8°) before the avalanche reached the north ridge (Figure 11a). Using Equation (7) leads to a slope angle θ=arctan(A_{v1}/A_{h1})=8.7°. In fact, the maximum slope angle from the Digital Elevation Model is about 10° and the mean slope at the beginning of the flow is about 4-5°, i.e. much smaller than the slope

angle for the Montserrat debris avalanche. Using Equation (11) and friction coefficients required to simulate such a large event (μ= tan(5°)=0.09) [e.g. see Kelfoun and Druitt, 2005, Lucas et al., 2013] gives M=1.6 F_h, which gives M=6.4×10^{12} kg. This is very similar to the estimated mass of the Mount St. Helens debris avalanche. Indeed, the estimated volume of the avalanche was 2.8×10^9 m^3, so that, with a density ρ=2000 kg/m^3, the estimated mass is M=5.6×10^{12} kg. No specific density is given for this event but the density of rocks is about 2500 kg/m^3 and the maximum volume fraction of monodisperse beads is about 0.6 while it can be higher than 0.9 for highly polydisperse materials because small particles can fill the pore space between larger particles [e.g. Voivret et al., 2007]. If we assume a volume fraction of 0.8, the density of the mass is 2000 kg/m^3. Note that we find here a quite different empirical factor between M and F_h (M=1.6 F_h) than the factor 0.54 proposed by Ekström and Stark [2013]. Our results suggest that relations (7) and (11) make it possible to roughly estimate the mass of a debris avalanche from the forces it generates.

The rough duration of the force (about 180 s ~3 minutes) is about the duration expected for the Mount St. Helens debris avalanche (about 150 s) [Kanamori et al., 1984]. If we assume that the duration of the landslide can be roughly estimated as twice the time interval between the two horizontal impulse forces (see Figure 1d), which is 90 s, the landslide duration might be about 180 s.

Using these values of the mass in Equations (13)-(14) gives a mean velocity of U=70.5 m/s and a center of mass travel distance L=12.7 km. Using Equation (15), we find R=19.7 km. Field observations suggests a velocity of 50 m/s<U<70 m/s and a runout distance of R≈26 km [Glicken 1986]. For the Mount St. Helens debris avalanche, the deposit is very extended so that we expect a significant difference between the center of mass travel distance L and the runout distance R.

5. Discussion

5.1 Main results for the two avalanches

For both models the azimuth of the force determined from the seismic data is opposite to the main azimuth of the avalanche flow as shown in Figures 2a and 11a, so that the flow direction can be recovered from the calculated force. Furthermore, our results suggest that the amplitude of the horizontal and vertical components of the force makes it possible to estimate the mass of the destabilized material and the slope of the topography during the initial avalanche motion while the time delays between the impulse forces can be considered to be about half the total duration of the landslide. From these characteristics, it was possible to estimate an average landslide velocity and travel distance of the center of mass. For both the Montserrat and Mount St. Helens debris avalanches, all these calculated quantities are of the same order of magnitude as those estimated from field observations.

For the Mount St. Helens case, the amplitudes of the vertical impulses are much smaller than those of the horizontal impulses. This may be due to the gentle slope over which the avalanche flowed. On the other hand, for the 1997 Montserrat event, the vertical force could not be ignored, the vertical downward amplitude being even slightly larger than that of the horizontal impulses, as was observed for the Mount Steller rock-ice avalanche (Figure 3a-c in Moretti et al., [2012]). The force models for the two debris avalanches reveal different features for horizontal and vertical components (Figure 9 and Figure 13). While the first horizontal and the first vertical impulses have been set at the same time to simplify the model, the second impulses are not simultaneous in the horizontal and vertical directions. In both cases here, the second vertical downward force occurs before the second horizontal impulse force. Note that for neither of the avalanches, it was possible to find a model fitting the data when the time of the second impulse was imposed to be the same for the horizontal and vertical components. The

ratios of A_{h2}/A_{h1}, A_{v1}/A_{v2} and A_{h1}/A_{v2} are also different. As a result, the horizontal and the vertical component from the same landslide event do not share the same source time function. This is in agreement with the force found by inversion of seismic data or numerical modeling of landslides for several landslide events [Moretti et al., 2012; Allstadt., 2013].

5.2 Limitations

Because the landslide length is small compared to the wavelength of the seismic waves and to the distances to the seismic stations, we assume a point source force and do not consider the spatial distribution of the force that would have to be taken into account for shorter periods and smaller source-station distances.

Furthermore, this method is based on the simple view of a block sliding on a slope with additional degrees of freedom for the source time functions of the horizontal and vertical components of the force. Some landslides are however more complicated than this simple scheme. For example, centrifugal forces due to 3D topography effects, physical processes such as entrainment of material along the slope or multiple events would affect this simple source time function [Moretti et al. 2012, Allstadt, 2013]. Description of such processes would add more parameters, leading to excessive computational costs. Nevertheless, the calculation of the mass, flow direction, initial slope of the topography and mean velocity are based on the first impulses in the horizontal and vertical directions. This initial stage in the flow is not expected to change greatly for many landslides even though other processes would affect the flow further downslope. We used here impulse forces while sinusoidal curves may be better suited to represent acceleration/deceleration of the landslide [Brodsky et al., 2003]. The landslide characteristics deduced from our best force model might have been different if we had used smoother

curves. However, no major changes are expected due to the narrow frequency band investigated here and the associated filtering process.

6. Conclusion

We used Monte-Carlo inversion of seismic data to calculate the force applied to the ground by landslides in order to extract information on landslide characteristics (mass, direction, duration, mean velocity, travel distance and initial slope of the underlying topography). The objective was to develop a method capable of providing first order estimates of these characteristics without using any field data concerning the deposit or the underlying topography, so that the method can be applied to past events or to landslides occurring in remote or inaccessible areas. For such landslides, only a few seismic stations are generally available, sometimes with poor signal to noise ratios. This prevents waveform inversion without a priori information using dense broadband station distribution and high-quality data, considered as a necessary condition for a unique and well constrained inversion result.

The alternative method proposed here is to assume an impulse force model for seismic inversion with a horizontal and a vertical force, each made up of two opposite forces separated by different time delays. The proposed impulse model appears to contain the minimum complexity necessary to explain seismic data. Simpler models were unable to reproduce the observed seismic signal. In particular, we found that the horizontal and vertical force components do not always share the same source time function, contrary to what was assumed in some previous studies. We performed a model space exploration to find the model that best fits the actual data for two large landslides using at most two distant seismic stations in a narrow frequency band. In order to reduce the number of runs in the Monte-Carlo inversion, we used the characteristics of the radiation pattern and first determined some

parameters of the horizontal force from the transverse component of the seismic signal before determining the others from all the components of the seismic signal. Simulations of the seismic signal generated by the best force model for the two landslides agree well with seismic data.

Good agreement is also found between the force calculated with waveform inversion using only one seismic station and with the Monte Carlo sampling method. This may suggest that the waveform inversion for a single force using only one or two stations is actually quite well constrained. A great advantage of the Monte Carlo method used here compared to simple waveform inversion is that it provides estimates of the parameter dispersion around the best parameters values, giving insight into the confidence intervals around these values. The use of the Neighborhood algorithm instead of the Monte Carlo method would significantly reduce the computational time necessary for inversion and the design of a Bayesian method would help to quantify the errors and the trade-offs between the inverted parameters.

Furthermore, as opposed to waveform inversion in a narrow frequency band, our method makes it possible to calculate a force history simple enough to be used to recover basic landslide characteristics. Simple analytical and empirical relations borrowed from the sliding block model and granular flow and landslide studies made it possible to estimate the mass, duration, flow direction, initial slope of the underlying topography and mean velocity and center of mass travel distance from the best force model calculated from the inversion of seismic data. These estimates appear to agree well with field data for both the Montserrat and the Mount St. Helens debris avalanches.

While in the future better data coverage will generally favor the use of waveform inversion methods to recover the landslide force history from long-period seismic data, this method may be useful to analyze past aerial or submarine landslides or landslides in remote areas, often recorded by only a few stations in a narrow frequency band and with low signal to noise ratios. Furthermore this

method could be used to validate poorly constrained waveform inversions. The proposed method, associated with waveform inversion when possible, will help identify landslide characteristics worldwide over an extending period of time where seismic data have been recorded and study their link with records of external forcing such as climate, seismic or volcanic activity over this time period.

Acknowledgments. We thank Joan L. Latchman, Gaël Burgos, Martin Vallée and Jean-Pierre Vilotte for useful discussions. This work was supported by ANR LANDQUAKES, the QUEST European Training network and the Seismological and Volcanological Observatories of IPGP.

References

Allstadt, K. (2013), Extracting Source Characteristics and Dynamics of the August 2010 Mount Meager Landslide from Broadband Seismograms, *J. Geophys. Res. Earth Surface*, 118(3), 1472-1490.

Bouchut, F., A. Mangeney-Castelnau, B. Perthame, and J. P. Vilotte (2003), A new model of Saint-Venant and Savage-Hutter type for gravity driven shallow water flows, C. R. *Acad. Sci. Paris*, Ser. I, 336, 531–536.

Brodsky, E. E., E. Gordeev, and H. Kanamori (2003), Landslide basal friction as measured by seismic waves, *Geophys. Res. Lett.*, 30(24), 2236, doi:10.1029/2003GL018485.

Chen, X., P. M. Shearer, F. Walter, and H. A. Fricker (2011), Seventeen Antarctic seismic events detected by global surface waves and a possible link to calving events from satellite images, *J.*

Geophys. Res., doi:10.1029/2011JB008262.

Christiansen, R.L., D. W. Peterson (1981), Chronology of the 1980 Eruptive activity, The 1980 Eruptions of Mount St. Helens, Washington: *U.S. Geological Survey Professional Paper* 1250, 844p

Dziewonski, A. M., and D. L. Anderson (1981), Preliminary reference Earth model, Physics of The Earth and Planetary Interiors, 25 (4), 297-356.

Ekström, G., M. Nettles, and G. A. Abers (2003), Glacial Earthquakes, *Science*, 302 (5645), 622-624.

Ekström, G., and Stark, C. P. (2013). Simple Scaling of Catastrophic Landslide Dynamics, *Science*, 339, 1416.

Farin, M., A. Mangeney, O. Roche (in review). Fundamental changes of granular flow dynamics, deposition and erosion processes at high slope angles: insights from laboratory experiments. J. *Geophys. Res.: Earth Surface*. *In review*

Favreau, P., Mangeney, A., Lucas, A., Crosta, G., and Bouchut, F. (2010), Numerical modeling of landquakes, *Geophys. Res. Lett.*, 37, L15305.

Gilbert, F., & Dziewonski, A. M. (1975). An application of normal mode theory to the retrieval of structural parameters and source mechanisms from seismic spectra. *Philosophical Transactions for the Royal Society of London. Series A, Mathematical and Physical Sciences*, 187-269.

Glicken, H. (1986). *Rockslide-debris avalanche of May 18, 1980, Mount St. Helens Volcano, Washington* (Doctoral dissertation, University of California, Santa Barbara.).

Hibert, C., Mangeney, A., Grandjean, G., & Shapiro, N. M. (2011). Slope instabilities in Dolomieu crater, Réunion Island: From seismic signals to rockfall characteristics. *Journal of Geophysical Research: Earth Surface (2003–2012)*,*116*(F4).

Kanamori, H., and J. W. Given (1982), Analysis of long-period seismic waves excited by the May 18, 1980, eruption of Mount St. Helens - a terrestrial monopole, *J. Geophys. Res.*, 87, 5422 – 5432.

Kanamori, H., J. W. Given, and T. Lay (1984), Analysis of seismic body waves excited by the Mount St. Helens eruption of May 18, 1980, *J. Geophys. Res.*, 89, 1856 – 1866.

Kawakatsu, H. (1989), Centroid single force inversion of seismic-waves generated by landslides, *J. Geophys. Res.*, 94(B9), 12,363 – 12,374.

Kelfoun, K., Druitt T.H., 2005, Numerical modeling of the emplacement of Socompa rock avalanche, Chile. *J. Geophys. Res.*, 110, B12202.

La Rocca, M., D. Galluzzo, G. Saccorotti, S. Tinti, G. B. Cimini, and E. D. Pezzo (2004), Seismic signals associated with landslides and with a tsunami at Stromboli Volcano, Italy, *Bulletin of the Seismological Society of America*, Vol. 94, No. 5, pp. 1850–1867.

Legros, F. (2002). The mobility of long-runout landslides. *Engineering Geology*,*63*(3), 301-331.

Lin, C. H., H. Kumagai, M. Ando, and T. C. Shin (2010), Detection of landslides and submarine slumps using broadband seismic networks, *J. Geophys. Res.*, VOL. 37, L22309, doi:10.1029/2010GL044685.

Lucas, A., Mangeney, A., and Ampuero, J. P., (2013). Frictional weakening in landslides on Earth and on other planetary bodies, *Geology*, submitted.

Mangeney-Castelnau, A., Vilotte, J. P., Bristeau, M. O., Perthame, B., Bouchut, F., Simeoni, C., & Yerneni, S. (2003). Numerical modeling of avalanches based on Saint Venant equations using a kinetic scheme. *Journal of Geophysical Research*, *108*(B11), 2527.

Mangeney, A., F. Bouchut, N. Thomas, J. P. Vilotte, and M. O. Bristeau (2007), Numerical modeling of self-channeling granular flows and of their levee-channel deposits, *J. Geophys. Res.*, 112, F02017, doi:10.1029/2006JF000469

Moretti, L., Mangeney, A., Capdeville, Y., Stutzmann, E., Christian Huggel, C., Schneider, D., and Francois Bouchut, F., (2012). Numerical modeling of the Mount Steller landslide flow history and of the generated long period seismic waves, *Geophys. Res. Lett.*, 39, L16402.

Petley, D. (2011). Damming events at Attabad. *International Water Power and Dam*

Construction, *63*(2), 27-29.

Roche, O., S. Montserrat, Y. Ni\~no, and A. Tamburrino (2008). Experimental observations of water-like behavior of initially fluidized, unsteady dense granular flows and their relevance for the propagation of pyroclastic flows. *J. Geophys. Res.*, 113, B12203.

Pirulli, M., and Mangeney, A., 2008. Result of Back-Analysis of the Propagation of Rock Avalanches as a Function of the Assumed Rheology, *Rock Mech. Rock Eng., 41(1), 59-84*.

Sambridge, M., & Mosegaard, K. (2002). Monte Carlo methods in geophysical inverse problems. *Reviews of Geophysics*, *40*(3), 3-1.

Sparks, R. S. J., J. Barclay, E. S. Calder, R. A. Head, J.-C. Komorowski, R. Luckett, G. E. Norton, L. J. Ritchie, B. Voight, and A. W. Woods (2002), Generation of a debris avalanche and violent pyroclastic density current on 26 December (Boxing Day) 1997 at Soufrière Hills Volcano, Montserrat in *The Eruption of Soufrière Hills Volcano, Montserrat, from 1995 to 1999. Geological Society, London, Memoirs*, 21, 409-434.

Tarantola, A. (2005). *Inverse problem theory and methods for model parameter estimation*. SIAM.

Tsai, V. C., and G. Ekström (2007), Analysis of glacial earthquakes, *J. Geophys. Res.*, 112, F03S22, doi:10.1029/2006JF000596.

Voight, B., Komorowski, J. C., Norton, G. E., Belousov, A. B., Belousova, M., Boudon, G., Francis, P.W., Franz, W., Heinrich, P., Sparks, R.S.J., Young, S. R. (2002). The 26 December (Boxing Day) 1997 sector collapse and debris avalanche at Soufriere Hills volcano, Montserrat. in *The Eruption of Soufrière Hills Volcano, Montserrat, from 1995 to 1999. Geological Society, London, Memoirs, 21*, 363-408.

Voivret, C., Radjai, F., Delenne, J.Y., El Youssoufi, M. S. (2007). Space-filling properties of polydisperse granular media, *Physical Review E*, 76, 021301, 2007.

Yamada, M., Y. Matsushi, M. Chigira, and J. Mori (2012), Seismic recordings of landslides caused by Typhoon Talas (2011), *Japan, Geophys. Res. Lett.*, 39, L13301 doi:10.1029/2012GL052174.

Yamada, M., H. Kumagai, Y. Matsushi, and T. Matsuzawa (2013), Dynamic landslide processes revealed by broadband seismic records, *Geophys. Res. Lett.*, 40, 2998–3002, doi:10.1002/grl.50437.

Figure 1. (a) Rigid block accelerating and decelerating down a slope and associated forces. (b) Force applied to the ground by a rigid block sliding over a 1D cross-section of the White River Valley, Montserrat (Equations (5)-(6)). (c) Force applied by a granular media spreading over a 1D cross-section of the White River Valley, Montserrat. The red circles represent the center of mass. This force was calculated using the SHALTOP model. (d) Schematic diagram of the horizontal and vertical pairs of opposite sign impulse forces used to perform the Monte-Carlo inversion. .

Figure 2. (a) Location of the Soufriere Hills Volcano (red dot) and the two MVO seismic stations with

short-period seismometers (red triangles). The light blue color marks out the area destroyed by the pyroclastic density current of the 26 December 1997 event in southern Montserrat. The dark gray area shows the deposits of the debris avalanche along the White River valley. The brown arrow represents the direction opposite to the inverted force that roughly corresponds to the avalanche flow direction. (b) Location of Montserrat (red circle) and the two seismic stations SJG and SDV with broad-band seismometers (red squares).

Figure 3. Seismogram and spectrogram of the seismic signal from the MVO stations in the frequency range 1-10 Hz (a) MBLG, (b) MBWH. The beginning of the six pulses observed in the signals is marked in red.

Figure 4. Spectrogram and selected seismic signals from stations SJG and SDV. The shaded area in each spectrogram shows the selected time duration (0-700 s) and period range (25-40 s) of the seismic signals shown in the gray rectangles below. (a) SJG transverse component. (b) SJG radial component. (c) SJG vertical component. (d) SJG particle motion in the radial/vertical direction. (e) SDV transverse component. (f) SDV radial component. (g) SDV vertical component. (h) SDV particle motion in the radial/vertical direction. For particle motion, the negative value corresponds to the direction toward the event.

Figure 5. Results of the waveform inversion for (a) the Montserrat debris avalanche, in the period 25-40s, using the seismic station SJG (black), SGJ and the vertical component of SDV (red) and for (b) the Mount St. Helens debris avalanche, in the period 100-250s, using the seismic stations ANMO (black), GRFO (red) and both stations (blue).

Figure 6. Radiation pattern produced by a force: The amplitude produced by a horizontal and a vertical force on the radial, transverse and vertical components of the seismogram recorded by a seismic station facing its azimuth. The star represents the position of the source. This figure shows that a signal recorded on the transverse component results only from the horizontal component of the force (green rectangle). The maximum amplitude of each component is given above each diagram. The amplitudes are relative to the maximum amplitude of the radial component corresponding to a horizontal force.

Figure 7. Results of the first step of the inversion for the Montserrat debris avalanche. The black stars mark where we have the maximum correlation value (a) Maximum correlation value between the transverse component of the synthetic and observed signals for different values of t_1. (b) Maximum correlation value between the transverse component of the synthetic and observed signals for different values of t_2-t_1 and A_{h2}/A_{h1} with a fixed t_1. (c) Maximum correlation value for different values of the azimuth, while the other parameters are fixed to t_1=80 s, t_2-t_1=69 s and A_{h2}/A_{h1}=-0.7.

Figure 8. Histograms of the parameters for the 10 best calculated models using correlation and misfit as constraints for the Montserrat inversion with three parameters fixed by using the transverse component of the seismic signal. Most of the parameters are well constrained, except A_{v2}/A_{h1} and A_{v1}/A_{v2}. The fixed parameters are: t_1=80 s, t_2-t_1=69 s and A_{h2}/A_{h1}=-0.7.

Figure 9. (a) Schematic representation of the best calculated force model for the Boxing Day debris avalanche, Montserrat. It shows the amplitude and the timing of each impulse force. (b) East, North and vertical components of the force corresponding to the best calculated model (i.e. source time function):

black lines correspond to the force model on the left filtered in the period 25-40 s; red lines are the result of the waveform inversion of the observed signal using the SJG station and the vertical component of the SDV station in the period 25-40 s.

Figure 10. Radial and transverse and vertical seismograms for the 26 December 1997 Montserrat event. Red lines show data seismograms, black lines show synthetic seismograms produced by the force time function calculated from the force model in Figure 9. (a) Station SJG. (b) Station SDV.

Figure 11. (a) Black curve shows the outline of crater, gray area shows the debris avalanche deposit distribution, red area shows the pyroclastic flow deposit distribution. The arrow represents the direction opposite to the inverted force. (b) The Northern hemisphere with the location of Mount St. Helens (red dot), and two seismic stations with broad-band seismometers (blue circles).

Figure 12. Histograms of the parameters for the 10 best calculated models using correlation and misfit as constraints for the Mount St. Helens inversion with three parameters fixed by using the transverse components of the seismic signal. Most of the parameters are well constrained, except A_{v2}/A_{h1} and t_3-t_1. The parameters fixed from the first step of the method are: t_1=65 s, t_2-t_1=90 s and A_{h2}/A_{h1}=-1.0

Figure 13. (a) Schematic representation of the best calculated force model for the Mount St. Helens debris avalanche. It shows the amplitude and the timing of each impulse force. (b) East, north and vertical components of the force source time function corresponding to the best calculated model on the left filtered in the period 100-250 s (black lines), red lines are from the waveform inversion of the observed signal at the closest station ANMO in the period 100-250 s, blue lines are from the waveform

inversion of the observed signal of both ANMO and GRFO seismic stations in the period 100-250 s.

Figure 14. Vertical, radial and transverse seismograms for the 18 May 1980 Mount St. Helens debris avalanche. Red lines represent the recorded seismograms in the period 100-250 s and black lines represents the synthetic seismograms produced by the force represented in Figure 13. (a) Station ANMO. (b) Station GRFO.

Table 1: Parameters exploration range.

Table 2: 10 best models, mean and standard deviation for the full model-space search, Montserrat.

Table 3: 10 best models, mean and standard deviation for the Method a, Montserrat.

Table 4: 10 best models, mean and standard deviation for the Method b, Montserrat.

Table 5: Best model's criteria values for different model-space exploration approaches, Montserrat.

Table 6: Best model's criteria values for different model-space exploration approaches, Mount St. Helens.

Figure 1
Click here to download high resolution image

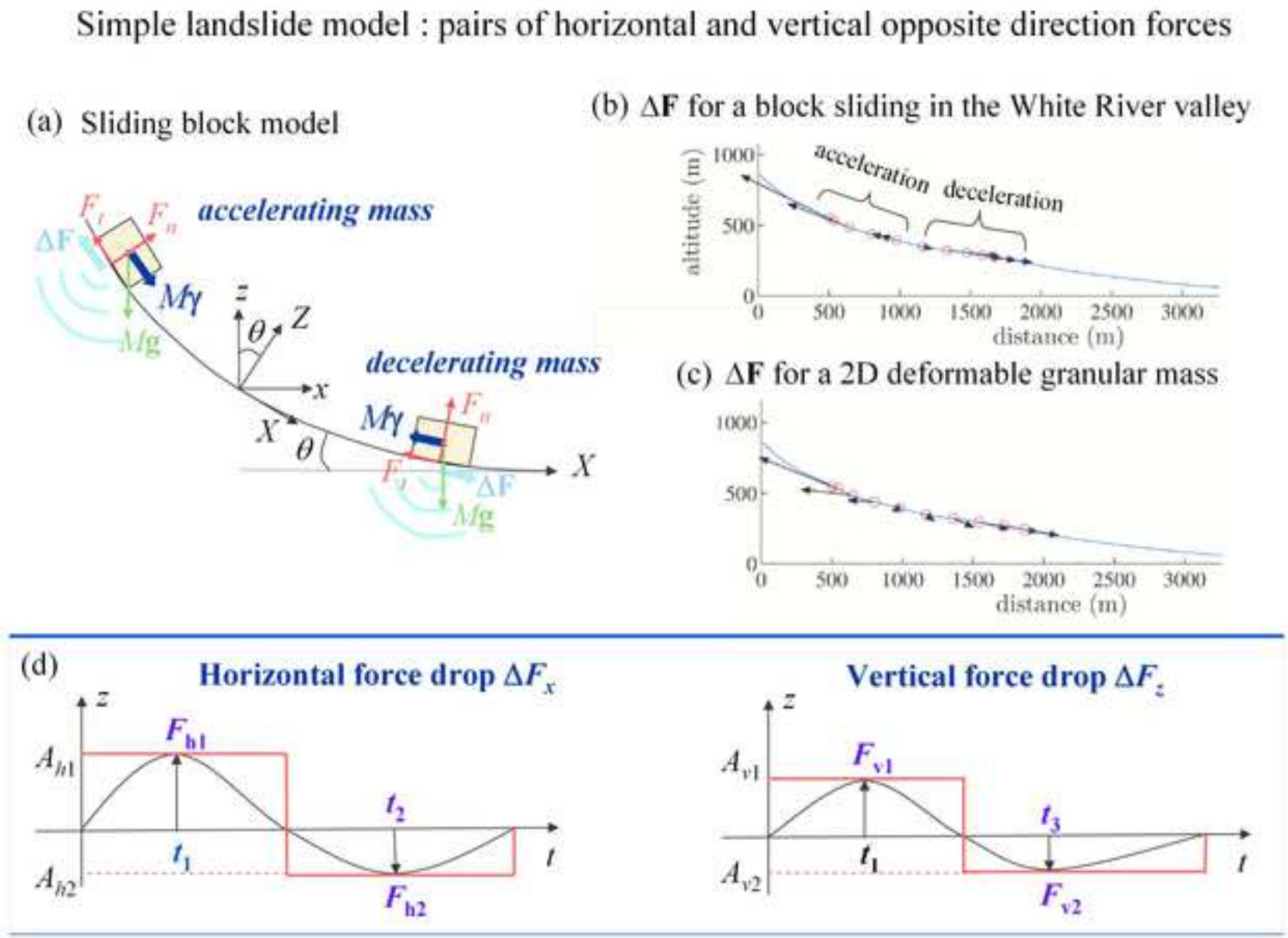

Figure 2
Click here to download high resolution image

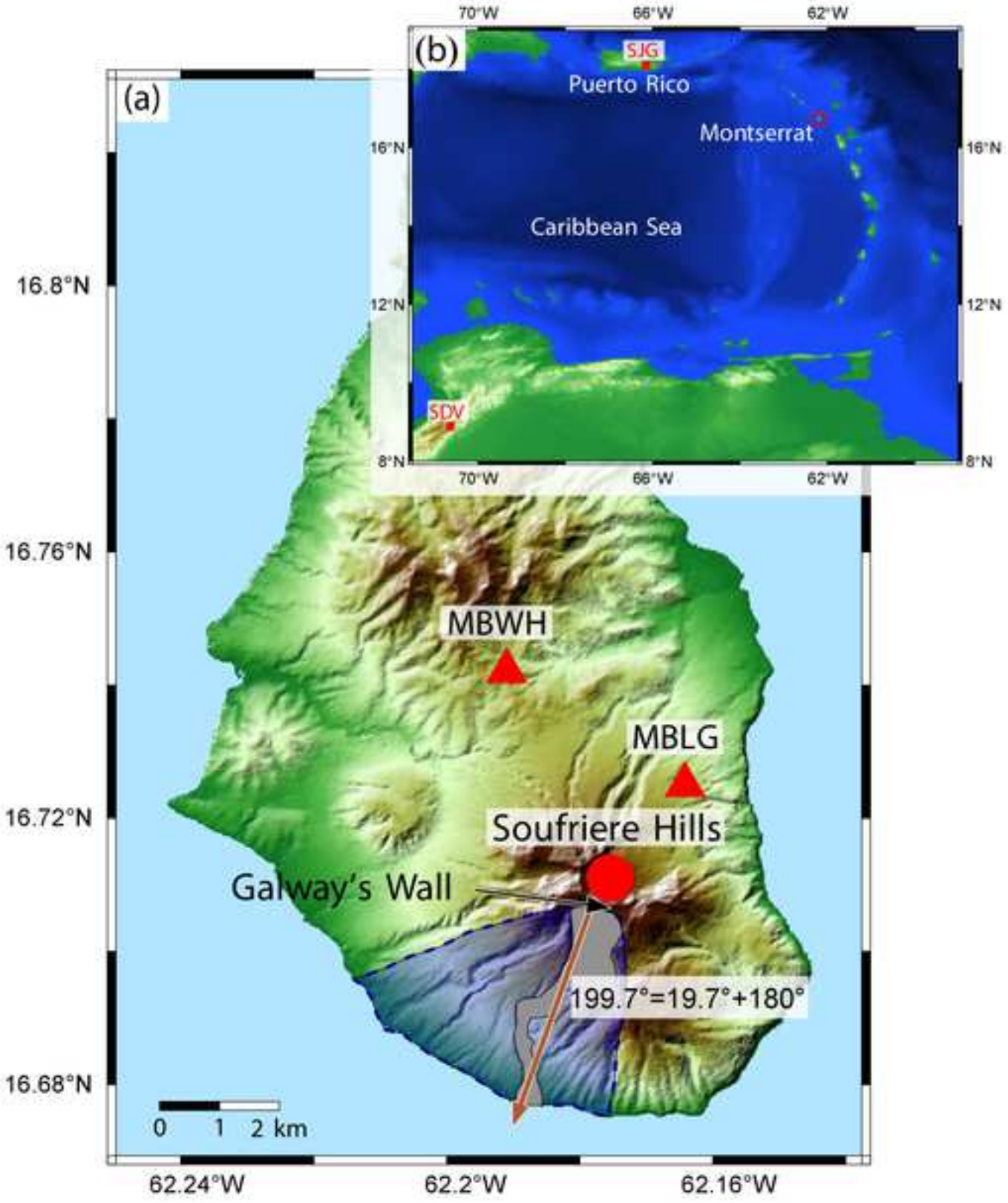

Figure 3
Click here to download high resolution image

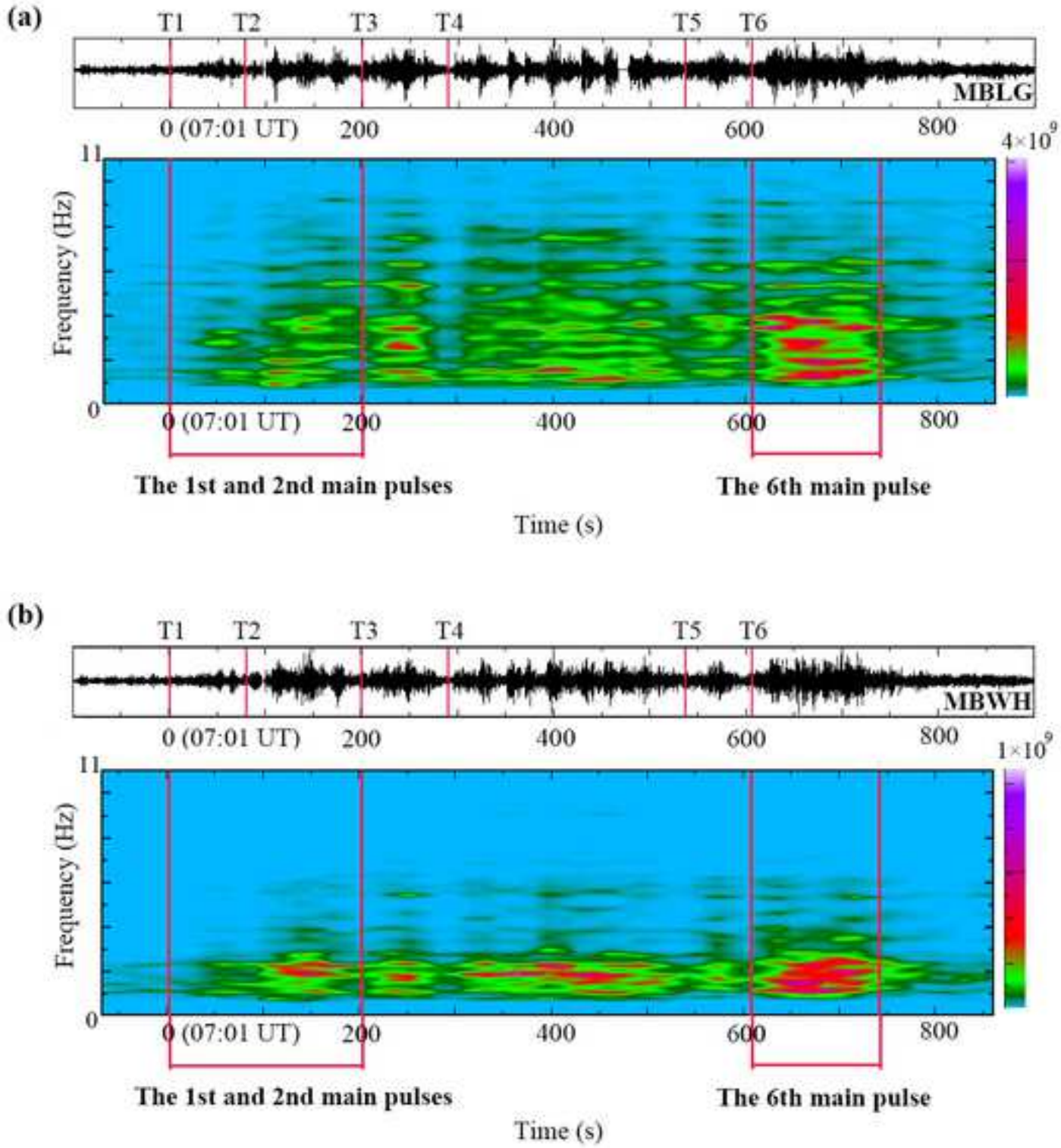

Figure 4

Click here to download high resolution image

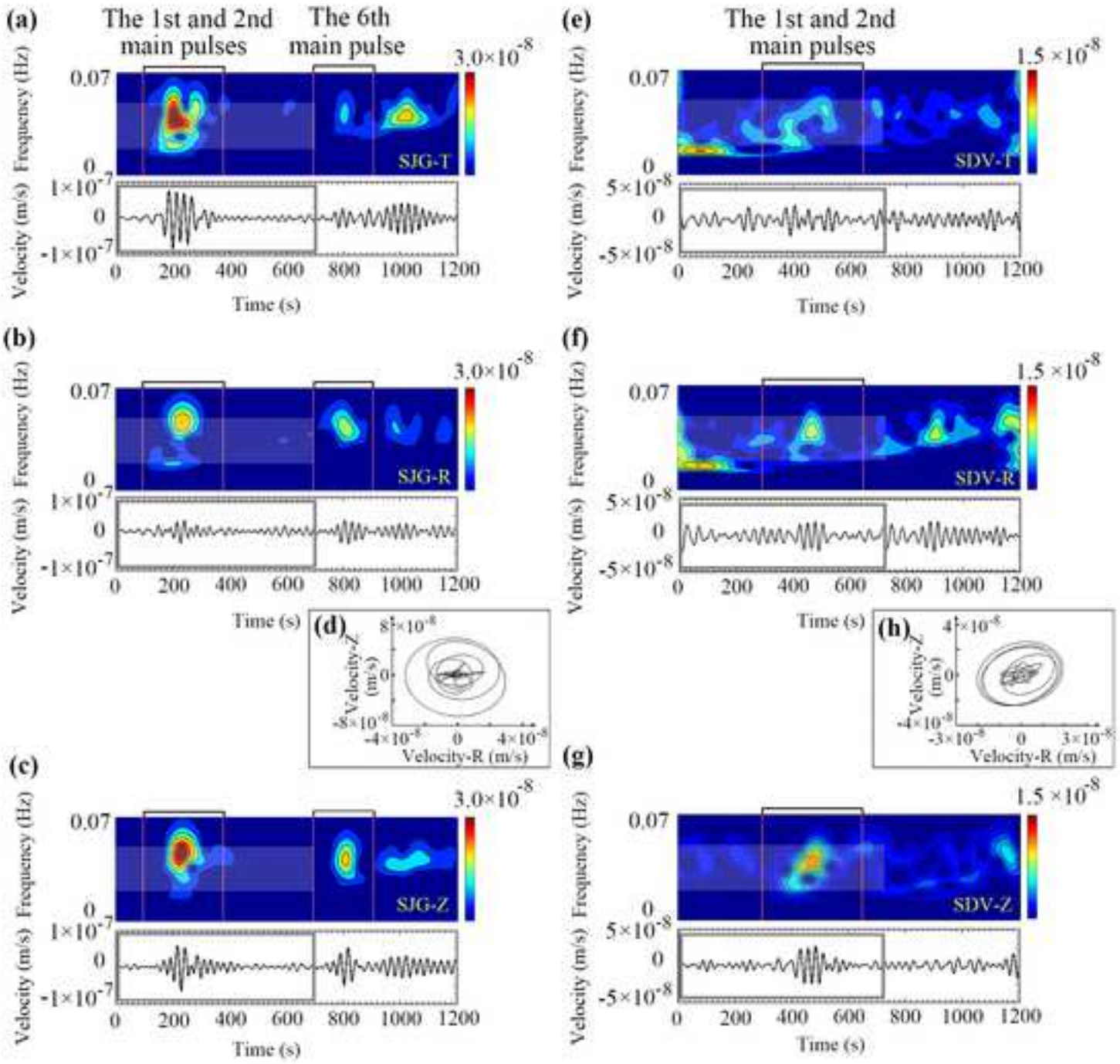

Figure 5

Click here to download high resolution image

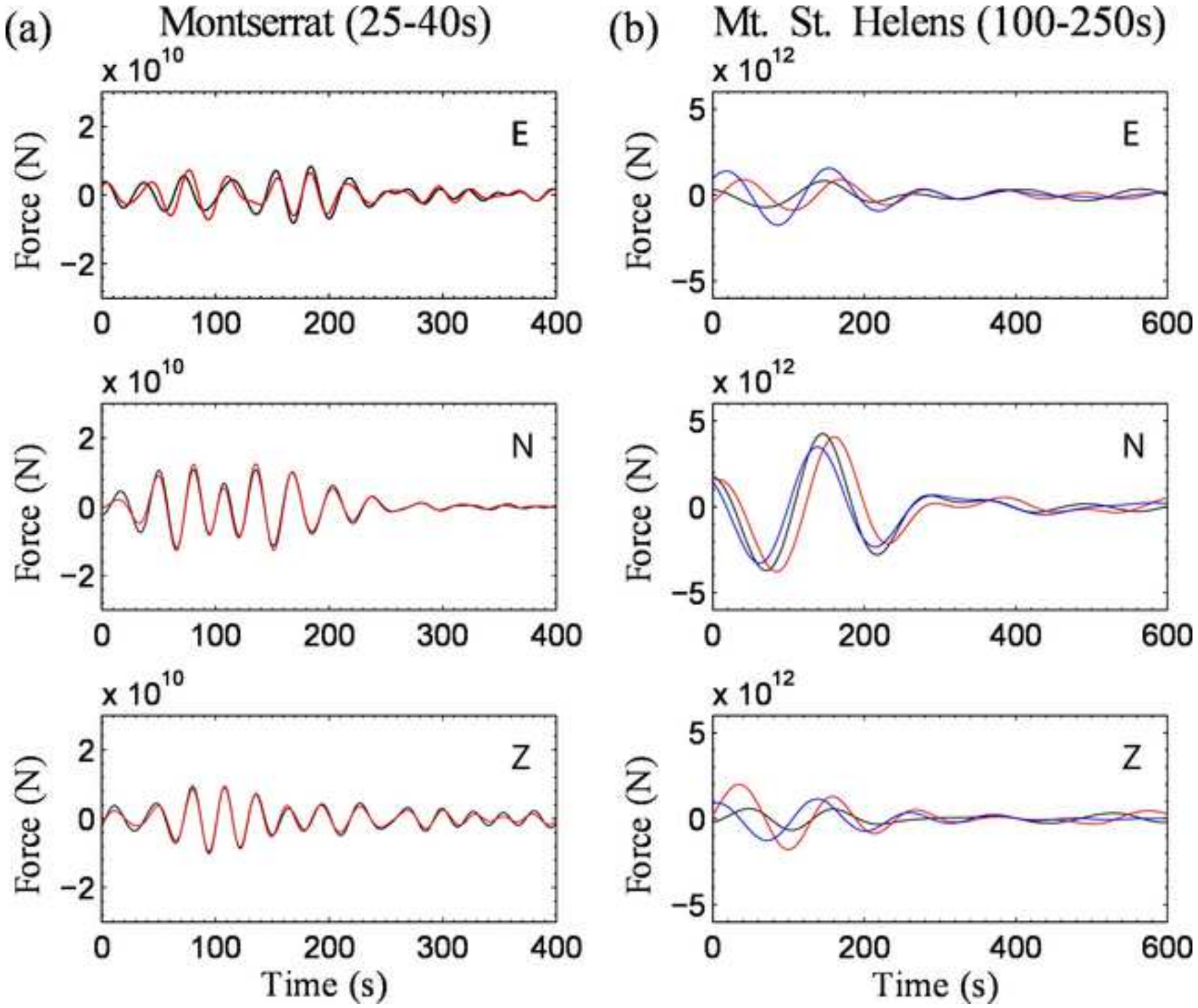

Figure 6
Click here to download high resolution image

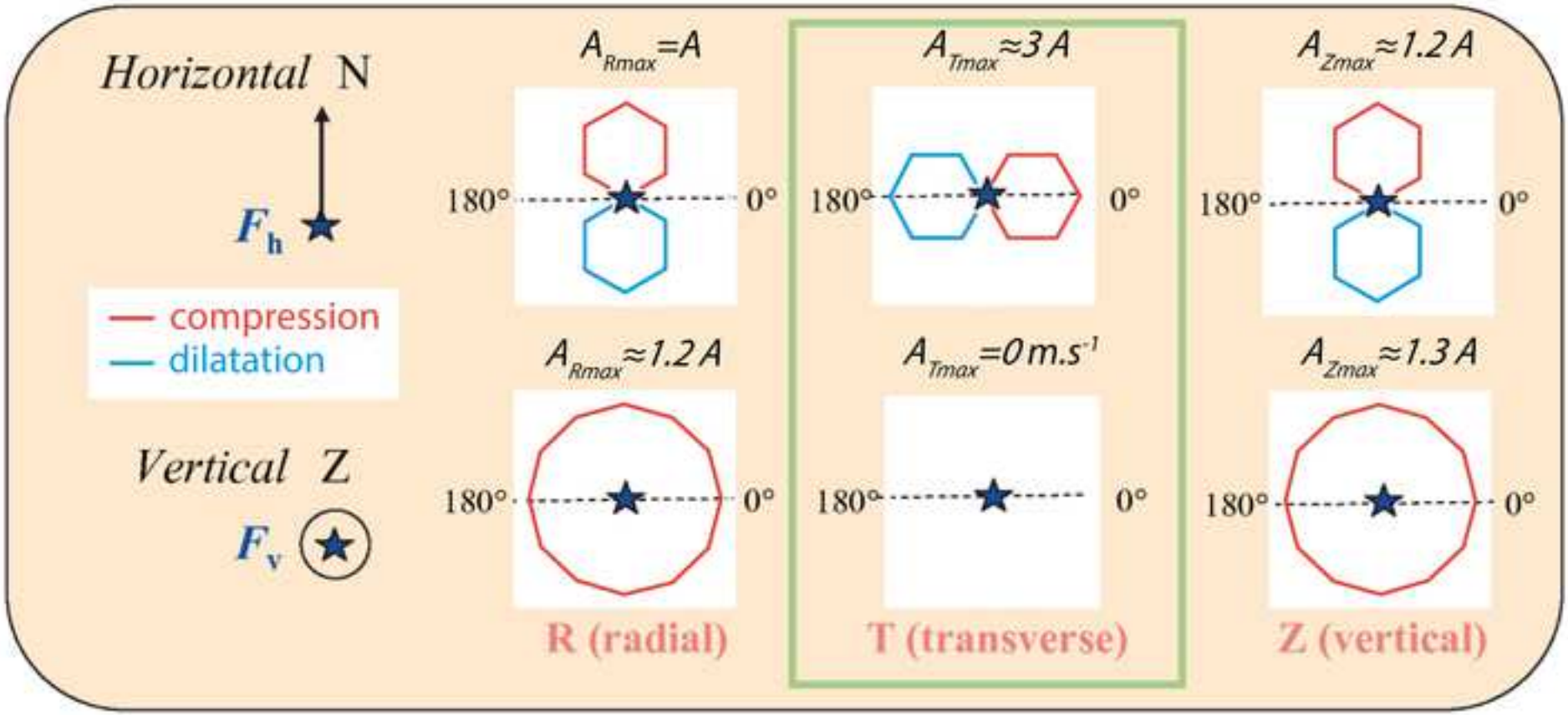

Figure 7
Click here to download high resolution image

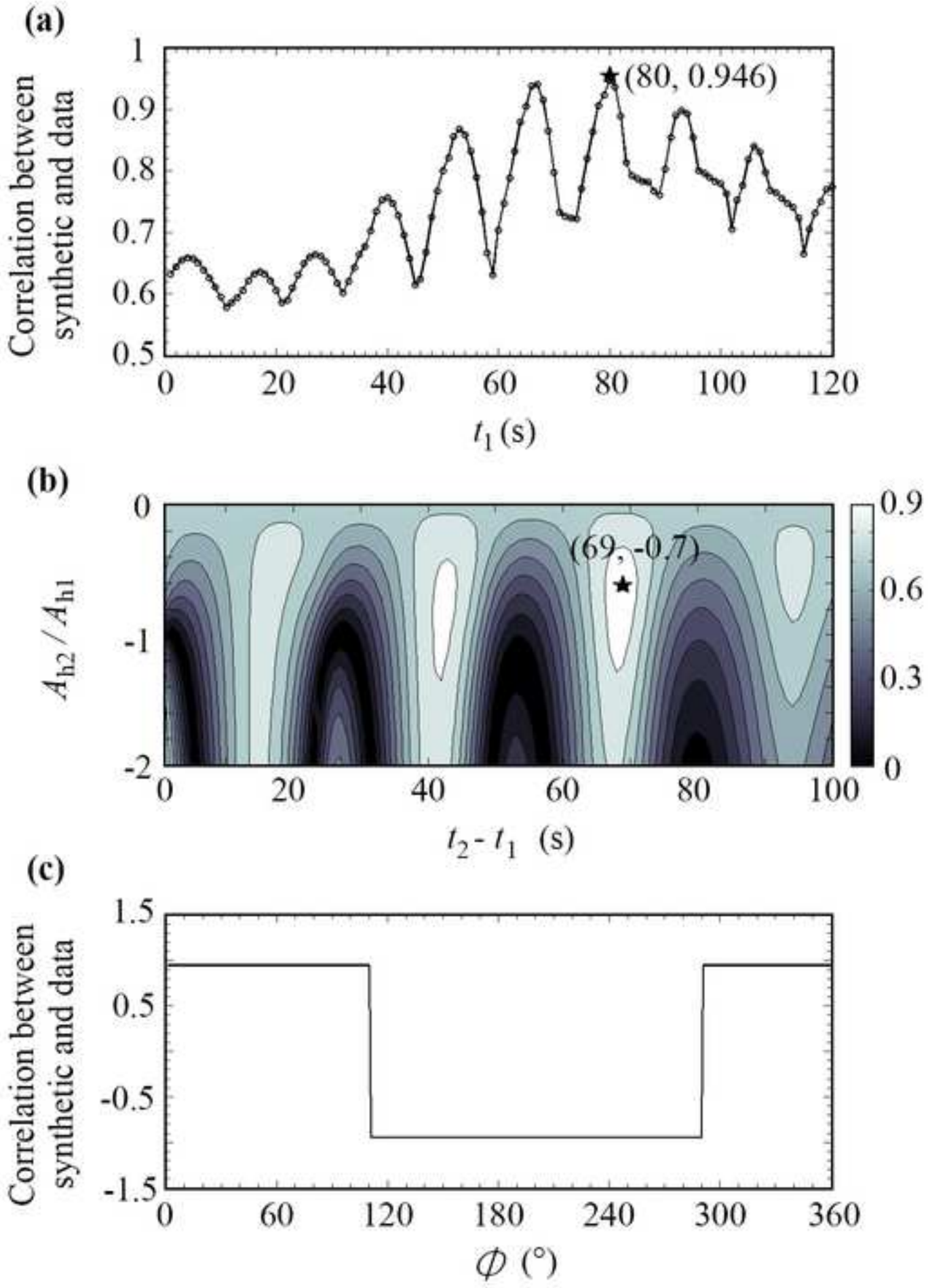

Figure 8

Click here to download high resolution image

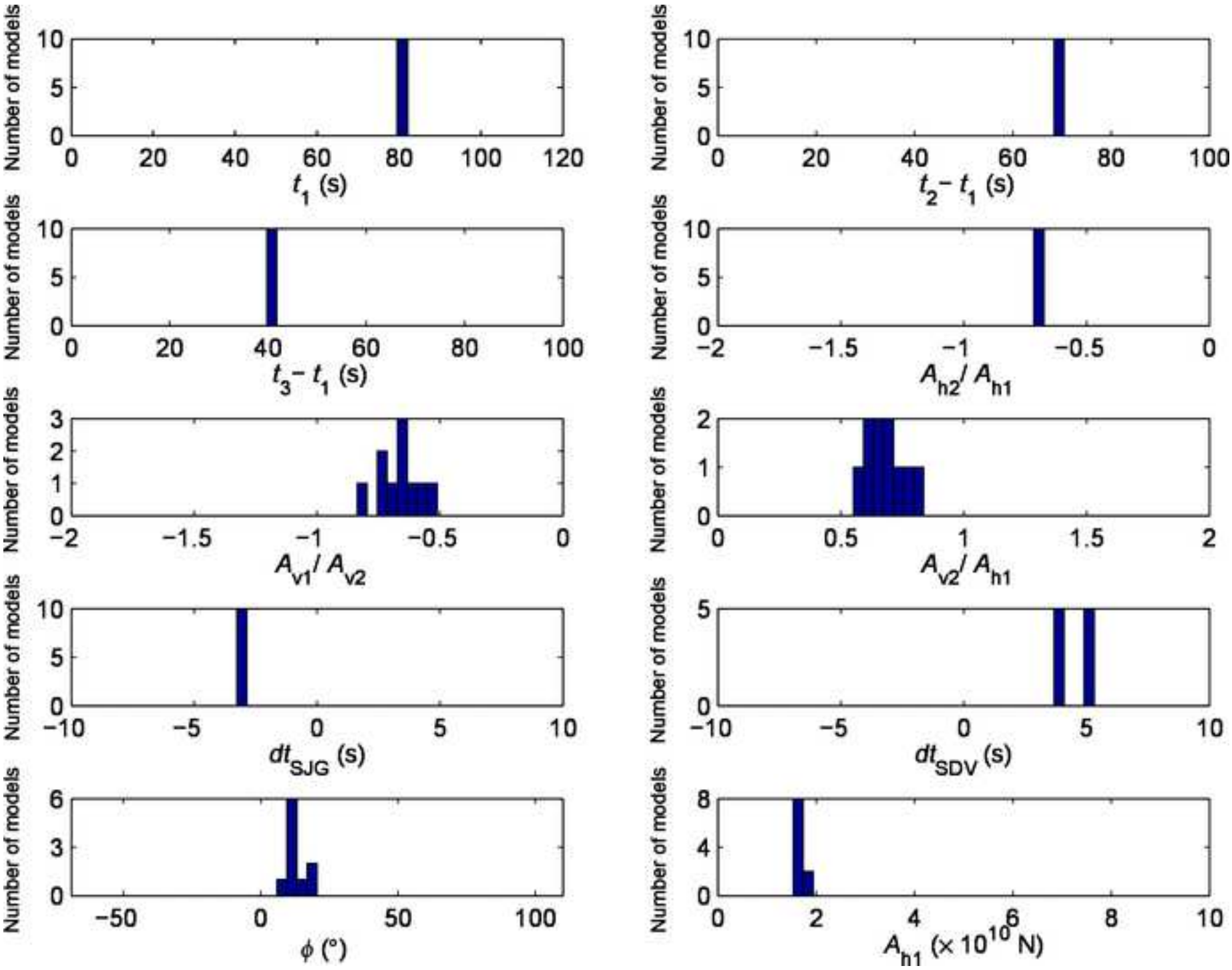

Figure 9
Click here to download high resolution image

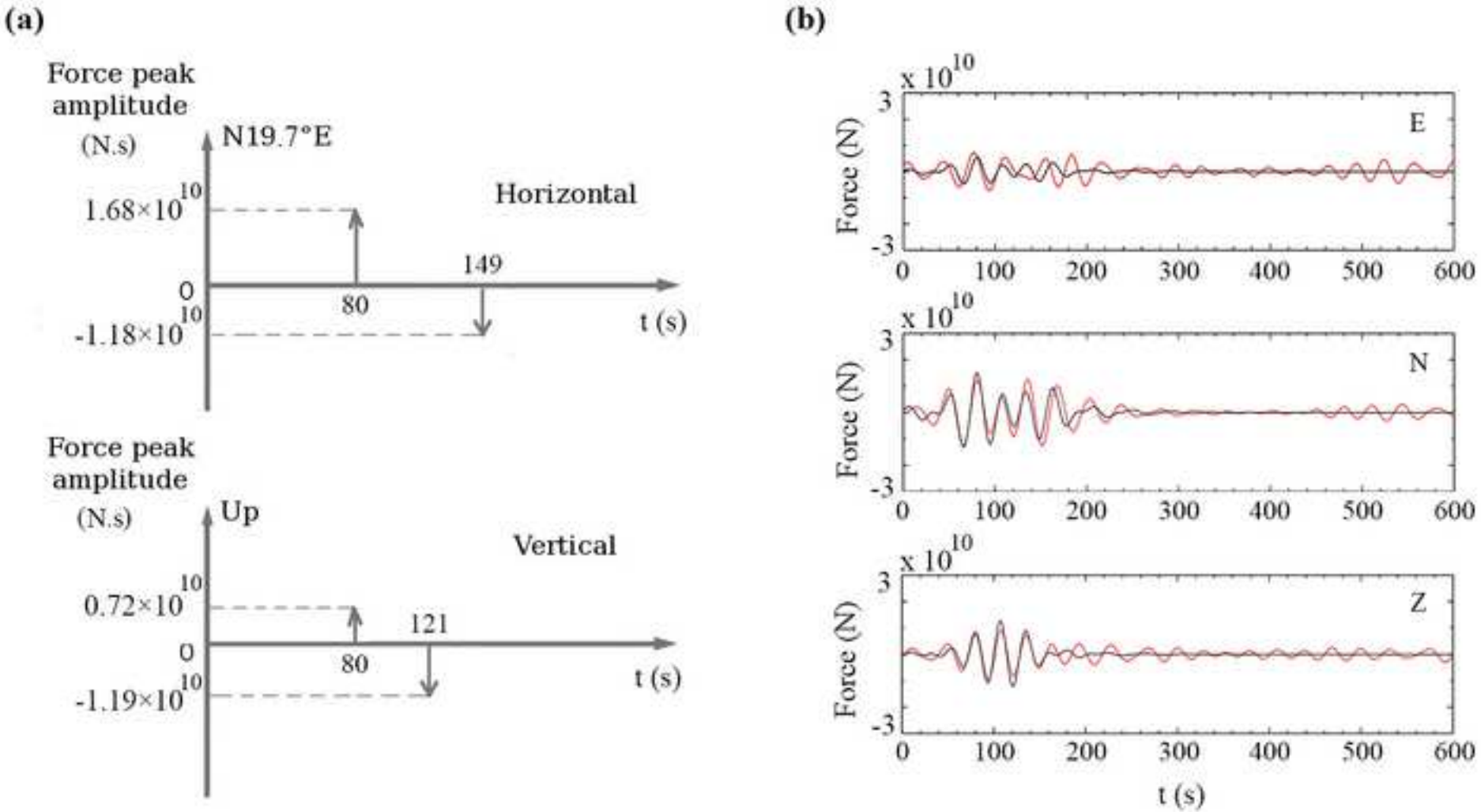

Figure 10
Click here to download high resolution image

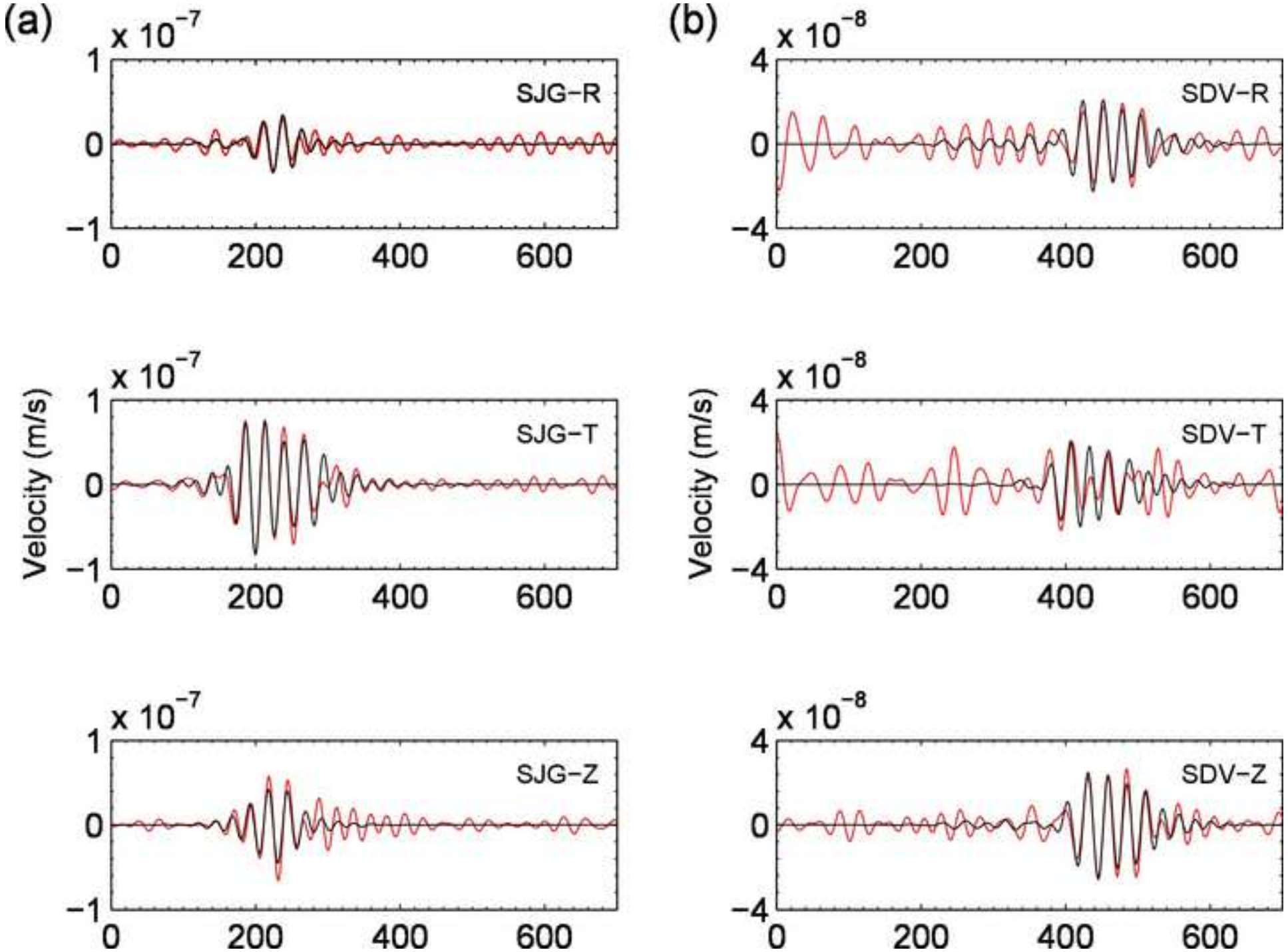

Figure 11
Click here to download high resolution image

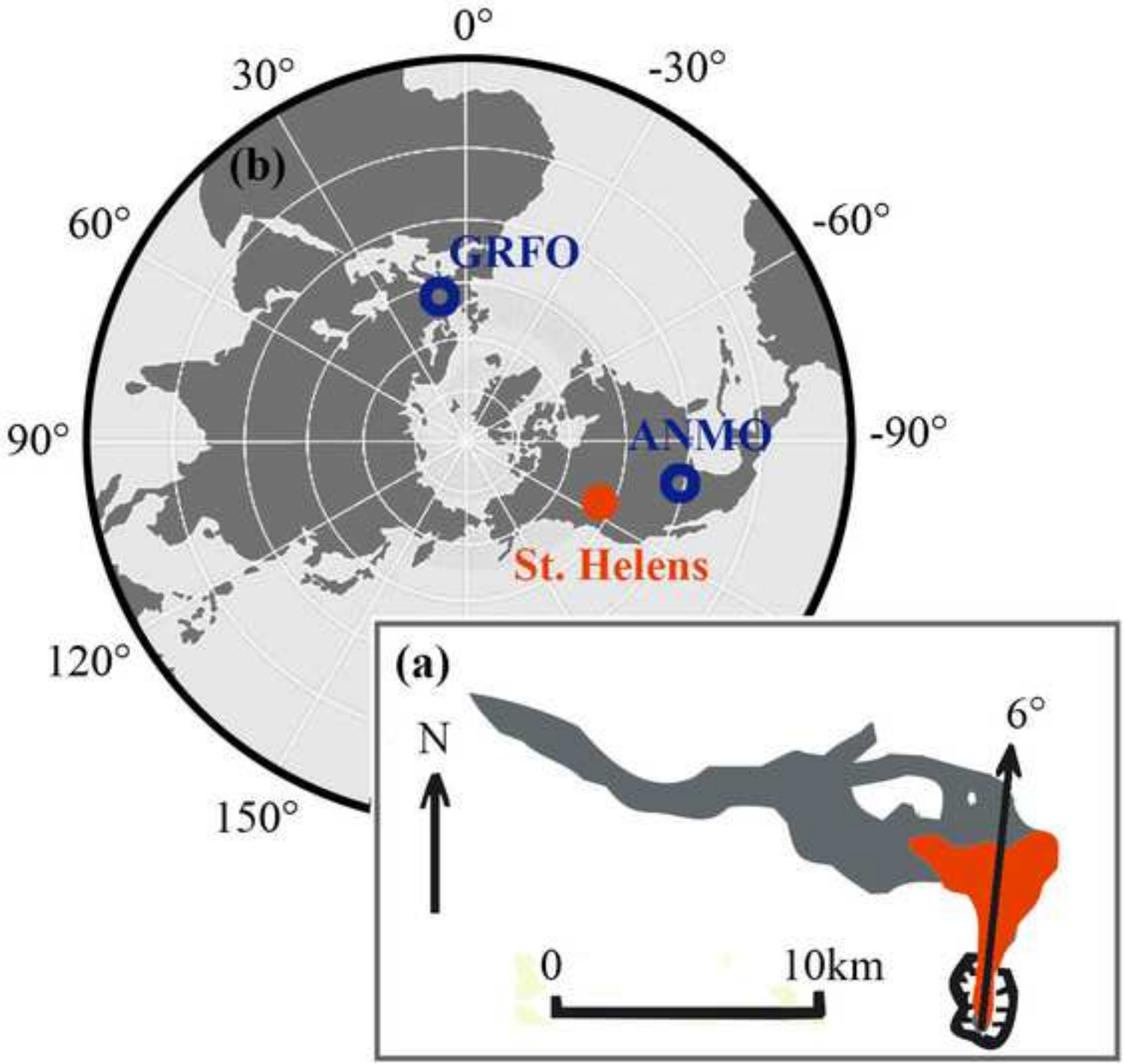

Figure 12
Click here to download high resolution image

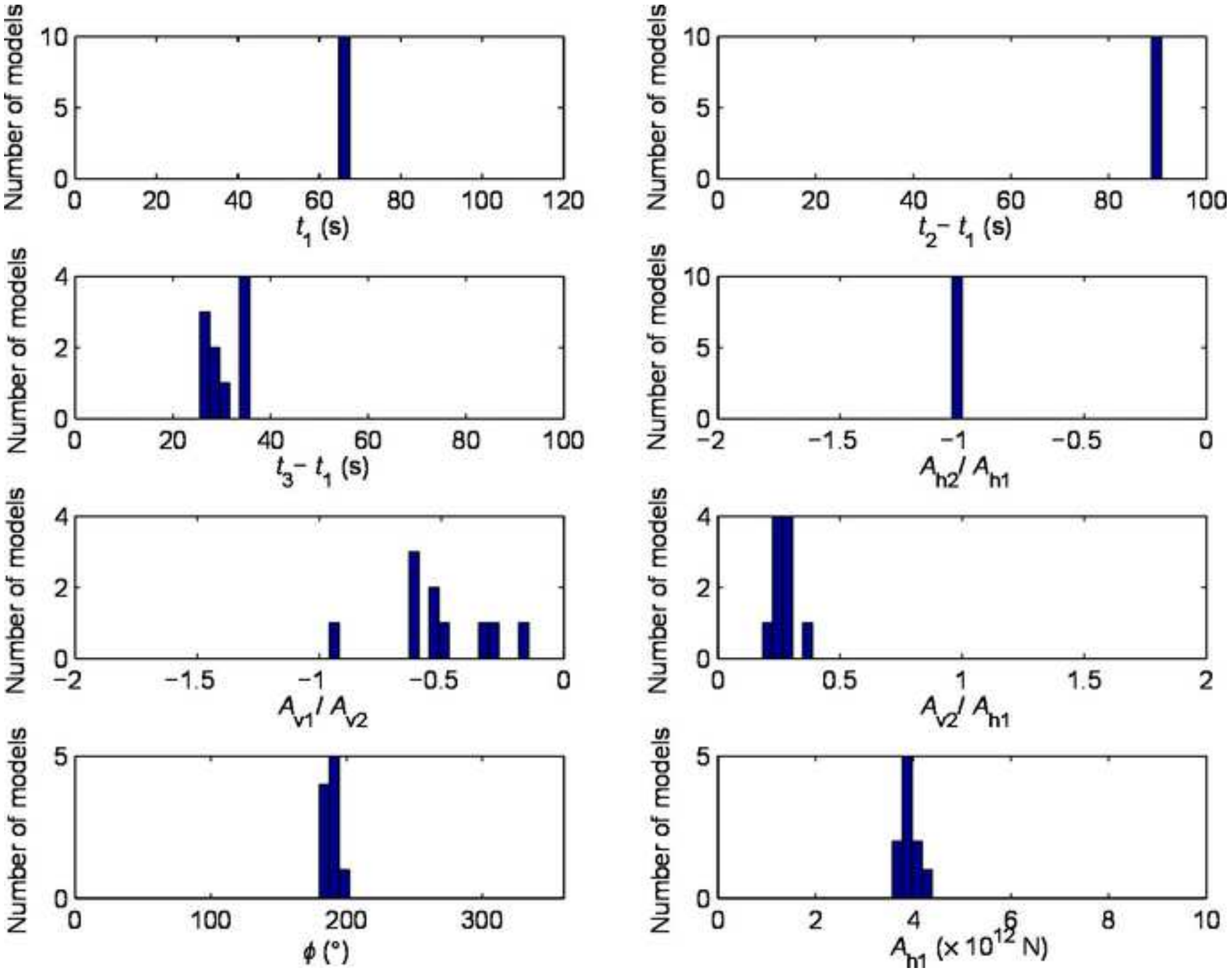

Figure 13
Click here to download high resolution image

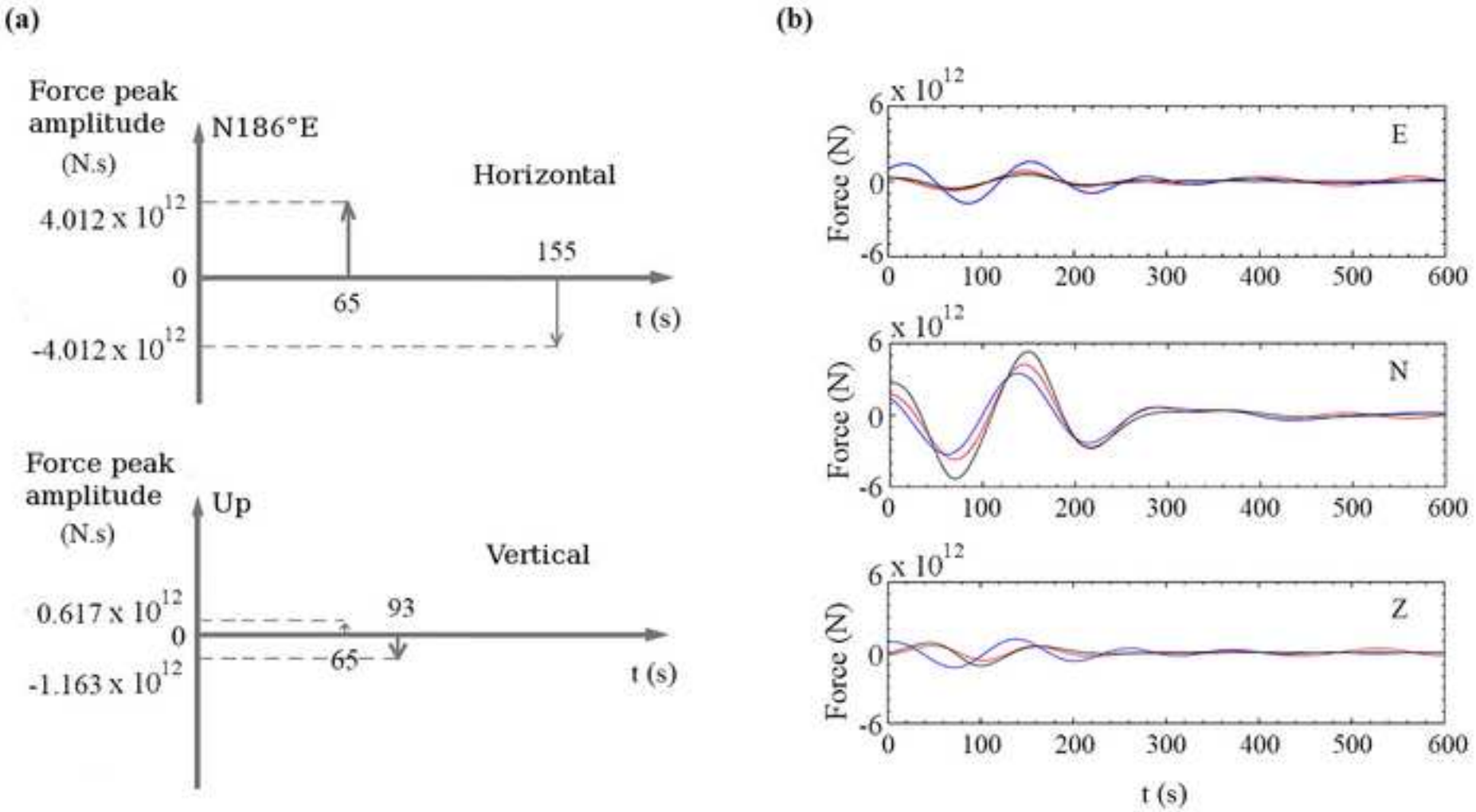

Figure 14
Click here to download high resolution image

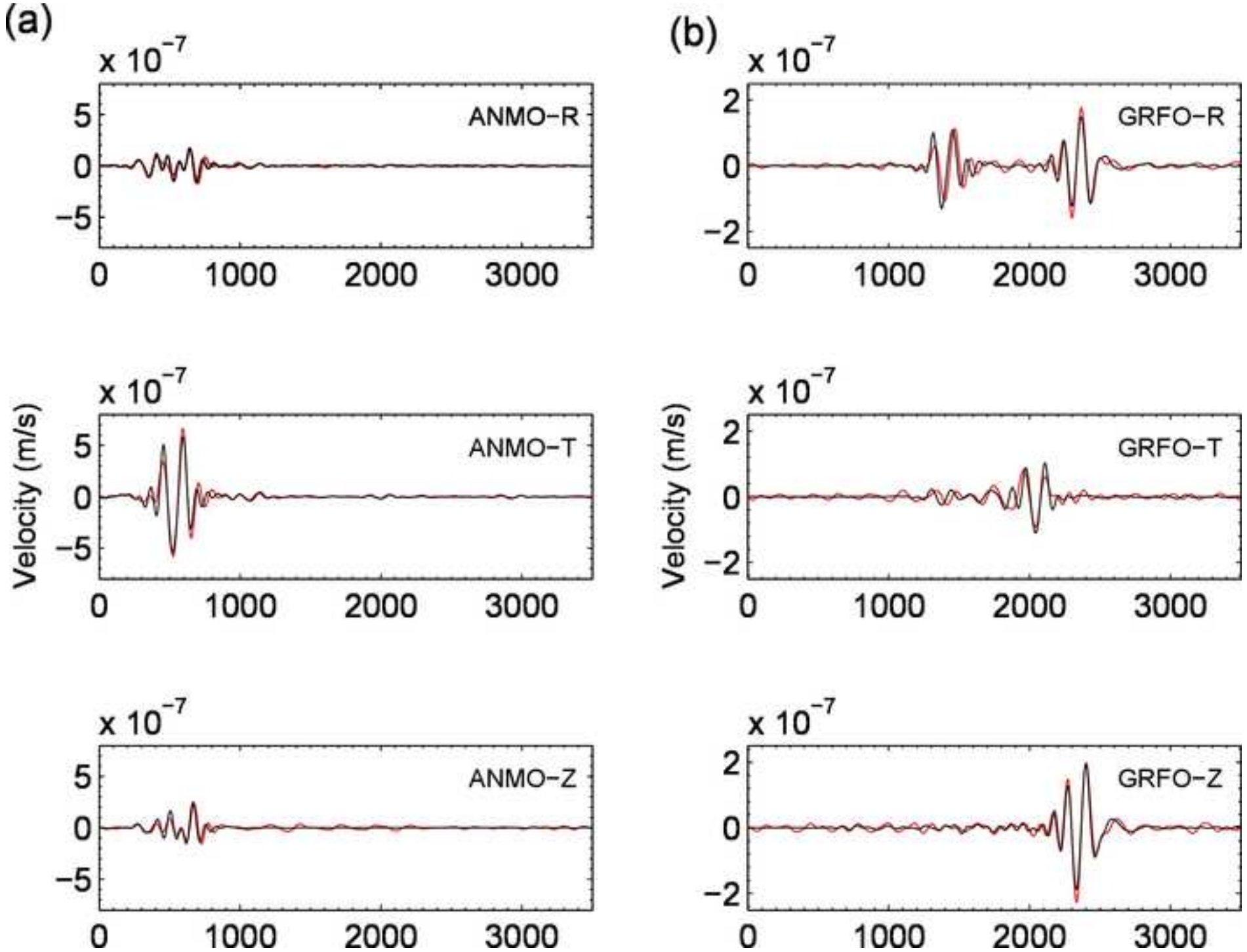

Table 1
Click here to download Table: Table_1.docx

Parameter	Exploration range (Montserrat)	Exploration range (Mount St. Helens)
t_1	[0,120]s	[0,120]s
t_2-t_1	[0,100]s	[0,120]s
t_3-t_1	[0,100]s	[0,120]s
A_{h1}	[0.5,10] $\times 1.10^{10}$ N	[1,10] $\times 1.10^{12}$ N
A_{h2}/A_{h1}	[-2,0]	[-2,0]
A_{v1}/A_{v2}	[-2,0]	[-2,0]
A_{v2}/A_{h1}	[0,2]	[0,2]
ϕ	[0,360]°	[0,360]°
dt	[-10,10]s (SJG)	[-50,50]s (ANMO)
dt	[-10,10]s (SDV)	[-50,50]s (GRFO)

Table 2

Click here to download Table: Table_2.docx

	t_1 (s)	t_2-t_1 (s)	t_3-t_1 (s)	A_{h2}/A_{h1}	A_{v2}/A_{h1}	A_{v1}/A_{v2}	dt_{SJG} (s)	dt_{SDV} (s)	ϕ (°)	A_{h1} ($\times 1.10^{10}$N)
Best model	80	43	40	-0.74	0.50	-0.89	-1	6	26.94	1.67
2nd model	82	44	40	-0.35	0.80	-0.82	-4	2	27.96	1.39
3rd model	81	43	41	-0.89	0.90	-0.67	-4	4	5.42	1.14
4nd model	80	42	38	-0.47	1.04	-0.63	0	6	12.10	1.35
5nd model	82	68	37	-0.72	0.35	-0.83	-3	6	10.28	2.32
6th model	83	68	36	-0.79	0.75	-0.50	-2	4	14.26	1.82
7th model	78	45	41	-1.0	1.15	-0.72	0	6	28.08	0.93
8th model	107	43	12	-0.64	0.59	-1.43	-3	4	16.49	1.38
9th model	79	43	35	-0.59	0.87	-0.46	2	8	19.91	1.09
10th model	82	70	37	-0.84	1.10	-0.85	-2	3	8.73	1.03
mean	82.69	55.08	36.85	-0.70	0.78	-0.71	-2.15	4.69	16.01	1.50
Standard deviation	7.43	13.28	7.76	0.17	0.23	0.33	1.91	1.60	7.49	0.40

Table 3
Click here to download Table: Table_3.docx

	t_1 (s) (fixed)	t_2-t_1 (s) (fixed)	t_3-t_1 (s)	A_{h2}/A_{h1} (fixed)	A_{v2}/A_{h1}	A_{v1}/A_{v2}	dt_{SJG} (s)	dt_{SDV} (s)	ϕ (°)	A_{h1} ($\times 1.10^{10}$N)
Best model	80	69	41	-0.7	0.71	-0.60	-3	5	19.74	1.68
2nd model	80	69	41	-0.7	0.57	-0.68	-3	5	11.20	1.67
3rd model	80	69	41	-0.7	0.72	-0.64	-3	4	10.81	1.72
4nd model	80	69	41	-0.7	0.62	-0.75	-3	5	16.22	1.68
5nd model	80	69	41	-0.7	0.67	-0.58	-3	4	12.05	1.61
6th model	80	69	41	-0.7	0.67	-0.72	-3	4	8.09	1.68
7th model	80	69	41	-0.7	0.67	-0.67	-3	4	18.23	1.67
8th model	80	69	41	-0.7	0.78	-0.67	-3	4	12.95	1.74
9th model	80	69	41	-0.7	0.62	-0.84	-3	5	12.91	1.60
10th model	80	69	41	-0.7	0.81	-0.53	-3	5	11.21	1.76
Mean	80	69	41	-0.7	0.68	-0.67	-3	4.5	13.24	1.68
Standard deviation	0	0	0	0	0.07	0.09	0	0.5	3.49	0.05

Table 4
Click here to download Table: Table_4.docx

	t_1 (s) (fixed)	t_2-t_1 (s) (fixed)	t_3-t_1 (s)	A_{h2}/A_{h1} (fixed)	A_{v2}/A_{h1}	A_{v1}/A_{v2}	dt_{SJG} (s)	dt_{SDV} (s)	ϕ (°)	A_{h1} ($\times 1.10^{10}$N)
Best model	80	69	40	-0.7	1.07	-0.30	-3	4	11	1.8
2nd model	80	69	40	-0.7	1.07	-0.30	-3	4	12	1.8
3rd model	80	69	40	-0.7	1.11	-0.20	-3	4	12	1.8
4nd model	80	69	39	-0.7	1.04	-0.40	-2	5	11	1.8
5nd model	80	69	40	-0.7	1.04	-0.40	-3	4	11	1.8
6th model	80	69	39	-0.7	1.07	-0.30	-2	5	11	1.8
7th model	80	69	39	-0.7	1.07	-0.30	-2	5	12	1.8
8th model	80	69	39	-0.7	1.07	-0.30	-2	5	13	1.8
9th model	80	69	39	-0.7	0.93	-0.20	-2	5	14	1.8
10th model	80	69	39	-0.7	0.93	-0.10	-2	5	14	1.8
mean	80	69	39.4	-0.7	1.04	-0.28	-2.4	4.6	12.1	1.8
Standard deviation	0	0	0.52	0	0.06	0.09	0.51	0.52	1.20	0

Table 5
Click here to download Table: Table_5.docx

	Correlation (SJG-R)	misfit (SJG-R)($\times 10^{-8}$)	Correlation (SJG-T)	misfit (SJG-T)($\times 10^{-8}$)	Correlation (SJG-Z)	misfit (SJG-Z)($\times 10^{-8}$)	Correlation (SDV-Z)	misfit (SDV-Z) ($\times 10^{-8}$)
Full model-space exploration	0.81	0.72	0.91	1.63	0.90	1.14	0.87	0.55
Method a (correlation and misfit)	0.82	0.73	0.95	1.19	0.90	1.06	0.93	0.40
Method b (correlation and amplitude ratio)	0.80	1.03	0.95	1.20	0.90	1.04	0.92	0.49

Table 6
Click here to download Table: Table_6.docx

	Correlation (ANMO-R)	misfit (ANMO-R)($\times 10^{-8}$)	Correlation (ANMO-T)	misfit (ANMO-T)($\times 10^{-8}$)	Correlation (ANMO-Z)	misfit (ANMO-Z)($\times 10^{-8}$)	Correlation (GRFO-R)	misfit (GRFO-R) ($\times 10^{-8}$)	Correlation (GRFO-T)	misfit (GRFO-T)($\times 10^{-8}$)	Correlation (GRFO-Z)	misfit (GRFO-Z) ($\times 10^{-8}$)
Method a	0.88	3.38	0.95	7.96	0.89	3.69	0.96	1.96	0.85	2.15	0.98	1.95
Method b	0.79	4.68	0.95	8.51	0.85	4.36	0.96	1.81	0.85	2.13	0.97	2.08

Supplementary Material

Click here to download Supplementary Material: supplementary_material.docx

Supplementary Material Figure 1

Click here to download Supplementary Material: S1.jpg

Supplementary Material Figure 2
Click here to download Supplementary Material: S2.jpg